AOA 377032

Quarterly Technical Report

Solid State Research

1999:4

Lincoln Laboratory

MASSACHUSETTS INSTITUTE OF TECHNOLOGY

LEXINGTON, MASSACHUSETTS

ADA 377032

This technical report has been reviewed and is approved for publication.

FOR THE COMMANDER

Gary Lutungian
Administrative Contracting Officer
Plans and Programs Directorate
Contracted Support Management

MASSACHUSETTS INSTITUTE OF TECHNOLOGY
LINCOLN LABORATORY

SOLID STATE RESEARCH

QUARTERLY TECHNICAL REPORT

1 AUGUST — 31 OCTOBER 1999

ISSUED 20 APRIL 2000

Approved for public release; distribution is unlimited.

LEXINGTON   MASSACHUSETTS

ABSTRACT

This report covers in detail the research work of the Solid State Division at Lincoln Laboratory for the period 1 August through 31 October 1999. The topics covered are Quantum Electronics, Electro-optical Materials and Devices, Submicrometer Technology, Biosensor and Molecular Technologies, Advanced Imaging Technology, Analog Device Technology, and Advanced Silicon Technology. Funding is provided by several DoD organizations—including the Air Force, Army, BMDO, DARPA, Navy, NSA, and OSD—and also by the DOE, NASA, and NIST.

TABLE OF CONTENTS

LIST OF ILLUSTRATIONS

LIST OF ILLUSTRATIONS (Continued)

LIST OF TABLES

INTRODUCTION

1. QUANTUM ELECTRONICS

Our work has demonstrated that an optically pumped 4-μm laser structure incorporating integrated absorber layers allows for the use of only a few quantum-well gain regions while providing sufficient pump absorption. The reduced optical confinement factor resulting from the use of only a few quantum wells directly reduces the carrier-induced antiguiding that the 4-μm mode experiences and increases beam brightness.

2. ELECTRO-OPTICAL MATERIALS AND DEVICES

The in-plane Seebeck coefficient, Hall coefficient, and electrical resistivity of PbSeTe/PbTe quantum-dot superlattice structures grown by molecular beam epitaxy have been measured at 300 K. The results have shown that a large enhancement of the in-plane Seebeck coefficient, thermoelectric power factor, and figure of merit has been achieved.

3. SUBMICROMETER TECHNOLOGY

Techniques have been developed to determine process modeling parameters for optical photoresists when exposed with an electron beam system. Predictions of feature size and the sensitivity of feature size to exposure dose have been verified experimentally for diazonaphthoquinone (DNQ)/novolac photoresists.

A novel trace vapor detector has been developed based on ion mobility spectroscopy using multiphoton uv laser ionization. This system achieves superior discrimination against certain interfering compounds such as amines, pyrroles, pyridines, pyrazines, and purines.

4. BIOSENSOR AND MOLECULAR TECHNOLOGIES

A novel sensor is being developed that uses biological membranes and ion channels to identify a wide variety of biological and chemical substances in a rapid, sensitive fashion. Applications of the sensor include biological/chemical agent detection, DNA analysis, medical diagnosis, and detection of drugs, explosives, or other chemicals of interest.

5. ADVANCED IMAGING TECHNOLOGY

The relationship between $1/f$ amplitude and upconverted phase noise has been investigated for n-type buried-channel MOSFET transistors. The measured results taken during the investigation, which indicate that a correlation exists between the $1/f$ amplitude and phase noise, may prove useful for reducing $1/f$ noise in the readout amplifier of charge-coupled devices.

6. ANALOG DEVICE TECHNOLOGY

Our study has shown that purification of Y_2O_3 may produce substantial improvements in microwave device efficiency at low temperatures. Transmission of microwave energy is critical to the efficiency of ferrites used in cryogenic control devices.

7. ADVANCED SILICON TECHNOLOGY

Initial work has been done on a method of modifying a deterministic parsing algorithm so that discourse-related analysis can be performed within the framework of the parse. This effort is a step toward computer understanding of natural language.

REPORTS ON SOLID STATE RESEARCH

1 AUGUST THROUGH 31 OCTOBER 1999

PUBLICATIONS

Low T_c Superconductive Circuits Fabricated on 150-mm-Diameter Wafers Using a Doubly Planarized $Nb/AlO_x/Nb$ Process	K. K. Berggren E. M. Macedo D. A. Feld J. P. Sage	*IEEE Trans. Appl. Supercond.* **9**, 3271 (1999)
Evaluation of Critical Current Density of $Nb/Al/AlO_x/Nb$ Josephson Junctions Using Test Structures at 300 K	K. K. Berggren M. O'Hara J. P. Sage A. H. Worsham*	*IEEE Trans. Appl. Supercond.* **9**, 3236 (1999)
Optical Materials and Coatings at 157 nm	T. M. Bloomstein V. Liberman M. Rothschild D. E. Hardy R. B. Goodman	*Proc. SPIE* **3676**, 342 (1999)
Molecular-Beam Epitaxial Regrowth on Oxygen-Implanted GaAs Substrates for Device Integration	C-L. Chen L. J. Mahoney S. D. Calawa K. M. Molvar P. A. Maki R. H. Mathews J. P. Sage T. C. L. G. Sollner	*Appl. Phys. Lett.* **74**, 4058 (1999)

---

*Author not at Lincoln Laboratory.

Screening of DNQ/Novolac Resists with E-Beam Exposure	T. H. Fedynyshyn S. P. Doran M. L. Lind T. M. Lyszczarz W. F. DiNatale D. Lennon C. Sauer* J. Meute*	*Proc. SPIE* **3678**, 1273 (1999)
Measurement of the Energy Sensitivity of a Superconductive Comparator	D. A. Feld J. P. Sage K. K. Berggren A. Siddiqui	*IEEE Trans. Appl. Supercond.* **9**, 4361 (1999)
Nanofabrication with Deep-Ultraviolet Lithography and Resolution Enhancements	M. Fritze S. Palmateer P. Maki J. Knecht C. K. Chen D. Astolfi S. Cann S. Denault K. Krohn P. W. Wyatt	*J. Vac. Sci. Technol. B* **17**, 3310 (1999)
Developments in X-Ray and Astonomical CCD Imagers	J. A. Gregory B. E. Burke B. B. Kosicki R. K. Reich	*Nucl. Instrum. Methods Phys. Res. A, Accel.* **436**, 1 (1999)

*Author not at Lincoln Laboratory.

PbTe/Te Superlattice Structures with Enhanced Thermoelectric Figures of Merit	T. C. Harman D. L. Spears M. P. Walsh	*J. Electron. Mater. Lett.* **28**, L1 (1999)
Surface Functionalization and Imaging Using Monolayers and Surface-Grafted Polymer Layers	M. D. K. Ingall* C. H. Honeyman* J. V. Mercure* P. A. Bianconi* R. R. Kunz	*J. Am. Chem. Soc.* **121**, 3607 (1999)
Modeling the Microwave Impedance of High-T_c Long Josephson Junctions	C. J. Lehner* D. E. Oates Y. M. Habib* G. Dresselhaus* M. S. Dresselhaus*	*J. Supercond.* **12**, 363 (1999)
Demonstration of Terahertz Water-Vapor Spectroscopy with a Photomixer Transceiver	K. A. McIntosh S. Verghese	*Proc. SPIE* **3794**, 16 (1999)
Magnetically Tunable Superconducting Resonators and Filters	D. E. Oates G. F. Dionne	*IEEE Trans. Appl. Supercond.* **9**, 4170 (1999)
Measurements and Modeling of Microwave Impedance of High-T_c Grain Boundaries	D. E. Oates Y. M. Habib* C. J. Lehner* L. R. Vale* R. H. Ono* G. Dresselhaus* M. S. Dresselhaus*	*IEEE Trans. Appl. Supercond.* **9**, 2446 (1999)

*Author not at Lincoln Laboratory.

A Nyquist-Rate Pipelined
Oversampling A/D Converter

S. A. Paul
H-S. Lee*
J. Goodrich*
T. F. Ala'ilima
D. D. Santiago

*IEEE International Solid-
State Circuits Conference:
Digest of Technical Papers*
(IEEE, Piscataway, N. J.,
1999), p. 54

First Demonstration of
Correlation in a Niobium
Superconductive Programmable
Binary-Analog Matched Filter

J. P. Sage
D. A. Feld

*IEEE Trans. Appl.
Supercond.* **9**, 4367
(1999)

Approaches to Designing
Thermally Stable Schottky
Contacts to n-GaN

H. S. Venugopalan*
S. E. Mohney*
J. M. DeLucca*
R. J. Molnar

Semicond. Sci. Technol.
14, 757 (1999)

High-Power High-Brightness
GaInAsSb-AlGaAsSb Tapered Laser
Arrays with Anamorphic Collimating
Lenses Emitting at 2.05 μm

J. N. Walpole
H-K. Choi
L. J. Missaggia
Z-L. Liau
M. K. Connors
G. W. Turner
M. J. Manfra
C. C. Cook

IEEE Photon. Technol. Lett.
11, 1223 (1999)

Extending the Cutoff Wavelength of
Lattice-Matched GaInAsSb/GaSb
Thermophotovoltaic Devices

C. A. Wang
H-K. Choi
D. C. Oakley
G. W. Charache*

*AIP Conference
Proceedings,* No. 460
(AIP Press, Woodbury, N.Y.,
1999), p. 256

High-Quantum-Efficiency 0.5 eV GaInAsSb/GaSb Thermophotovoltaic Devices	C. A. Wang H-K. Choi S. L. Ransom* G. W. Charache* L. R. Danielson* D. M. DePoy*	*Appl. Phys. Lett.* **75**, 1305 (1999)
Increase in Response Time of Low-Temperature-Grown GaAs Photoconductive Switches at High Voltage Bias	N. Zamdmer* Q. Hu* K. A. McIntosh S. Verghese	*Appl. Phys. Lett.* **75**, 2313 (1999)
Q-Switched Microchip Lasers Find Real-World Application	J. Zayhowski	*Laser Focus World* **35** (8), 129 (1999)

ACCEPTED FOR PUBLICATION

Outlook for Resist Design at 157 nm	R. R. Kunz T. M. Bloomstein T. H. Fedynyshyn	*J. Vac. Sci. Technol.*
Outgassing of Organic Vapors from 193-nm Photoresists: Impact on Atmospheric Purity Near the Lens Optics	R. R. Kunz D. K. Downs V. Liberman R. S. Uttaro	*J. Vac. Sci. Technol.*

---

*Author not at Lincoln Laboratory.

Materials Issues for Optical Components and Photomasks in 157-nm Lithography	V. Liberman M. Rothschild J. H. C. Sedlacek R. S. Uttaro A. K. Bates C. VanPeski T. M. Bloomstein	*J. Vac. Sci. Technol.*
HVPE-GaN Avalanche Photodiodes	K. A. McIntosh R. J. Molnar L. J. Mahoney S. Verghese	*Appl. Phys. Lett.*
Time-Resolved Photoluminescence Studies of Free and Donor-Bound Exciton in GaN Grown by Hydride Vapor Phase Epitaxy	R. J. Molnar G. E. Bunea* W. D. Herzog* M. S. Unlü* B. B. Goldberg*	*Appl. Phys. Lett.*
Low Frequency Noise in High Electron Mobility n-GaN	R. J. Molnar S. L. Rumyantsev* D. Look* M. E. Levinshtein* G. Simin* V. Adivarahan* M. S. Shur*	*J. Appl. Phys.*
Comparative Metrology Methods for Quantifying the Edge-Roughness of Straight Features in Resist and Silicon	C. Nelson S. C. Palmateer T. M. Lyszczarz	*J. Vac. Sci. Technol.*

*Author not at Lincoln Laboratory.

157 nm: The Deepest Deep-UV Yet	M. Rothschild	*J. Vac. Sci. Technol.*
High Power, High Brightness GaInAsSb-AlGaAsSb Tapered Laser Arrays with Anamorphic Collimating Lenses Emitting at 2.05 μm	J. N. Walpole H. K. Choi L. J. Missaggia Z. L. Liau M. K. Connors G. W. Turner M. J. Manfra C. C. Cook	*IEEE Photon. Technol. Lett.*

PRESENTATIONS[†]

Optical Sampling for Analog to Digital Conversion	P. W. Juodawlkis G. E. Betts J. C. Twichell J. L. Wasserman R. C. Williamson	DARPA/MTO '99 Optoelectronics Meeting Review, San Diego, California, 1-5 August 1999
Solar-Blind Avalanche Photodiodes	S. Verghese	DARPA/MTO '99 Optoelectronics Meeting Review, San Diego, California, 1-5 August 1999
Epitaxial Growth of GaInAsSb for Thermophotovoltaics	C. A. Wang	11th American Conference on Crystal Growth and Epitaxy, Tucson, Arizona, 1-6 August 1999

[†]Titles of presentations are listed for information only. No copies are available for distribution.

HVPE ELO-GaN Growth	R. J. Molnar A. Lightfoot L. J. Mahoney	Lateral Epitaxial Overgrowth Workshop, Juneau, Alaska, 2-5 August 1999
Self-Assembly in Epitaxial Semiconductor Alloys	C. A. Wang K. Rajan* Y. C. Chen* V. Bucklen* G. Nichols* M. Freeman* P. Sanders*	2nd International Conference on Alloys, Davos, Switzerland, 8-13 August 1999
Photon-Counting Two-Dimensional Geiger-Mode Avalanche Photodiode Array	B. B. Kosicki	1999 Meetings of the IRIS Specialty Groups on Materi- als and Detectors, MIT Lincoln Laboratory, Lexington, Massachusetts, 16-19 August 1999
A Study of Resist Outgassing as a Function of Differing Photoadditives	F. M. Houlihan* I. L. Rushkin* R. S. Hutton* A. G. Timko* O. Nalamasu* E. Reichmanis* A. H. Gabor* A. N. Medina S. G. Slater* S. Malik* R. R. Kunz D. K. Downs	American Chemical Society National Symposium, New Orleans, Louisiana, 22-26 August 1999

*Author not at Lincoln Laboratory.

PbTe-Based Quantum-Dot Thermoelectric Materials with High ZT	T. C. Harman P. J. Taylor D. L. Spears M. P. Walsh	International Conference on Thermoelectrics, Baltimore, Maryland, 29 August–9 September 1999
Sites and Motion of Mu Defect Centers in *n*-Type Gallium Nitride	R. J. Molnar R. L. Lichti* S. F. J. Cox* M. R. Dawdy* T. L. Head* B. Hitti* C. Schwab* R. I. Vaudo*	8th Conference on Muon Spin Rotation, Relaxation, and Resonance, Les Diablerets, Switzerland, 30 August–3 September 1999
Analog Devices	D. E. Oates	NATO ASI, Millau France, 30 August–10 September 1999
Epitaxial Growth of GaInAsSb for Thermophotovoltaics	C. A. Wang	3rd International Conference on Mid-IR Optoelectric Material and Devices, Aachen, Germany, 6-7 September 1999
Mobile Surface Electrons on Negative Electron Affinity Diamond	M. W. Geis K. E. Krohn N. N. Efremow J. M. Lawless, Jr. J. C. Twichell T. M. Lyszczarz	10th European Conference on Diamond, Diamond-Like Materials, Nitrides and Silicon Carbide, Prague, Czech Republic, 12-17 September 1999

*Author not at Lincoln Laboratory.

CCD Imager Development at MIT Lincoln Laboratory	B. B. Burke	ESO Optical Detector Workshop, Munich, Germany, 13-16 September 1999
A Comparison of DNQ/Novolac Resists with E-beam Exposure	T. H. Fedynyshyn S. P. Doran M. Lind T. M. Lyszczarz W. F. DiNatale D. M. Lennon C. Sauer* J. Meute*	19th Annual BACUS Symposium on Photomask Technology and Management, Monterey, California, 15-17 September 1999
Photolithography at Wavelengths Below 200 nm	M. Rothschild	Semiconductor Equipment and Materials International, New England Breakfast Forum, Burlington, Massachusetts, 22 September 1999; Optical Society of America Annual Meeting, Santa Clara, California, 26 September–1 October 1999
Laser Beam Combining for Power and Brightness Scaling	T. Y. Fan C. C. Cook A. Sanchez	Optical Society of America Annual Meeting, Santa Clara, California, 26 September–1 October 1999

*Author not at Lincoln Laboratory.

Outlook for 157-nm Resist Design	R. R. Kunz D. E. Hardy R. B. Goodman D. K. Downs J. E. Curtin T. M. Bloomstein	National Science Foundation/ Semiconductor Research Center and Engineering Rescarch Center Teleseminar, Lexington, Massachusetts, 30 September 1999
Superconductive Crossbar Circuits	K. Berggren D. A. Feld	Workshop on Superconducting Electronics, Rosendale, New York, 3-7 October 1999
Submicron, High-T_c Processing of Nb/AlO$_x$/Nb Trilayers at MIT Lincoln Laboratory	K. Berggren M. O'Hara D. A. Feld E. M. Macedo T. Weir	Workshop on Superconducting Electronics, Rosendale, New York, 3-7 October 1999
Low Frequency Noise in High Electron Mobility n-GaN	R. J. Molnar S. L. Rumyantsev* D. C. Look* M. E. Levinshtein* M. Asif Khan* G. Simin* V. Adivarahan* M. S. Shur*	International Conference on Silicon Carbide, Research Triangle Park, North Carolina, 10-15 October 1999
Optical Materials for 157 nm Lithography	M. Rothschild	2nd International UV Laser Symposium for 157 nm, Fort Lauderdale, Florida, 13-14 October 1999

---

*Author not at Lincoln Laboratory.

ORGANIZATION

SOLID STATE DIVISION

D. C. Shaver, *Head*
R. W. Ralston, *Associate Head*
N. L. DeMeo, Jr., *Assistant*
Z. J. Lemnios, *Senior Staff*

J. W. Caunt, *Assistant Staff*
K. J. Challberg, *Administrative Staff*
J. D. Pendergast, *Administrative Staff*

SUBMICROMETER TECHNOLOGY

M. Rothschild, *Leader*
T. M. Lyszczarz, *Assistant Leader*
T. H. Fedynyshyn, *Senior Staff*
R. R. Kunz, *Senior Staff*

Astolfi, D. K.	Liberman, V.
Bloomstein, T. M.	Maki, P. A.
DiNatale, W. F.	Palmacci, S. T.
Doran, S. P.	Palmateer, S. C.
Efremow, N. N., Jr.	Sedlacek, J. H. C.
Forte, A. R.	Spector, S. J.
Geis, M. W.	Sworin, M.
Goodman, R. B.	Uttaro, R. S.
Krohn, K. E.	

QUANTUM ELECTRONICS

A. Sanchez-Rubio, *Leader*
T. Y. Fan, *Assistant Leader*
T. H. Jeys, *Senior Staff*

Aggarwal, R. L.	DiCecca, S.
Buchter, S. C.	Goyal, A. K.
Cook, C. C.	O'Brien, P. W.
Daneu, J. L.	Ochoa, J. R.
Dancu, V.	Zayhowski, J. J.

ELECTRO-OPTICAL MATERIALS AND DEVICES

J. C. Twichell, *Leader*
D. L. Spears, *Assistant Leader**
G. W. Turner, *Assistant Leader*
H. K. Choi, *Senior Staff*
R. C. Williamson, *Senior Staff*

Bailey, R. J.	Juodawlkis, P. W.	Nitishin, P. M.
Betts, G. E.	Liau, Z. L.	Oakley, D. C.
Calawa, A. R.*	Lightfoot, A.	O'Donnell, F. J.
Calawa, D. R.	Mahoney, L. J.	Poillucci, R. J.
Calawa, S. D.	Manfra, M. J.	Taylor, P. J.
Connors, M. K.	McIntosh, K. A.	Verghese, S.
Donnelly, J. P.	Missaggia, L. J.	Walpole, J. N.
Goodhuc, W. D.	Molnar, R. J.	Wang, C. A.
Harman, T. C.	Mull, D. E.	Wasserman, J. L.
Harris, C. T.	Napoleone, A.	

*Part Time

1. QUANTUM ELECTRONICS

1.1 HIGH-BRIGHTNESS, QUANTUM-WELL MID-INFRARED SEMICONDUCTOR LASERS

Semiconductor lasers emitting in the mid-infrared (3–5 μm) region are of interest for a variety of commercial and military applications. Impressive advances have been made in increasing the output power from such lasers whether they be optically pumped [1],[2] or electrically pumped [3]. Using a quantum-well (QW) laser design which utilizes GaInAsSb integrated absorber regions, our group has recently demonstrated ~2-W single-facet peak output power from an optically pumped QW semiconductor laser operating at 77 K. In addition to high peak power, other key laser performance parameters affect their usefulness in practical applications. These include power efficiency, maximum average output power, maximum operating temperature, and brightness. Here, we show that the brightness of a QW laser which utilizes integrated absorber regions is much greater than that of the best double-heterostructure (DH) lasers [4] even though the peak output power is comparable. To our knowledge, no other group has quantified the brightness of their 4-μm semiconductor laser sources.

In optically pumped 4-μm lasers reported to date, the active gain region also serves to absorb the incident pump power. To absorb a large fraction of incident pump radiation, the active region is typically designed to be thick. For DH lasers, this means using a >1-μm-thick InAsSb active region. For QW devices, typically >50 quantum wells are used. Since the carrier-induced refractive index change in these 4-μm active regions is roughly 10× greater than that in typical GaAs-based lasers, the 4-μm optical mode experiences a strong antiguiding effect which degrades beam brightness. This antiguiding effect can be significantly reduced by designing a QW laser structure to have only a few QWs such that the overlap of the 4-μm mode with the active region is small. A reduced optical overlap with the active region, or confinement factor, is also advantageous in reducing filamentation [5]. Furthermore, the antiguiding parameter in QWs is significantly less than that in bulk active regions [6]. By incorporating an integrated-absorber region, which acts to absorb the ~2-μm pump radiation while remaining transparent to the 4-μm lasing mode, we are free to choose the number of QWs in the laser structure without regard to pump absorption. Here, we show that both the divergence angle and beam spot size in the junction plane of the laser (lateral dimension) is significantly reduced in a QW laser having only six QWs as compared to a DH laser.

The epitaxial layer structure for DH and QW lasers is schematically depicted in Figure 1-1. Both structures were grown on (100) n-GaSb substrates using solid-source molecular-beam epitaxy. The DH laser structure consists of a 1.5-μm InAs$_{0.91}$Sb$_{0.09}$ active region which is sandwiched between 2-μm-thick AlAs$_{0.08}$Sb$_{0.92}$ top and bottom optical cladding layers. The QW laser active region consists of five 23-Å InAs/24-Å GaInSb/23-Å InAs QWs which are each surrounded by GaInAsSb absorber layers such that the total absorber thickness is 0.925 μm. The top and bottom optical cladding layers (away from the active region) consist of 0.5-μm AlAs$_{0.08}$Sb$_{0.92}$, 0.5-μm GaSb, and 1.5-μm AlAs$_{0.08}$Sb$_{0.92}$. Both the DH and QW laser structures were capped with 100 Å of GaSb to protect the AlAsSb from oxidation. The overlap of the 4-μm optical mode with the active region is calculated to be 88% and 3% for the DH and QW lasers, respectively.

**Double
Heterostructure**

**Quantum
Well**

GaSb
10 nm

Top
Cladding

AlAsSb 2000 nm

AlAsSb 1500 nm

GaSb 500 nm

AlAsSb 500 nm

Waveguide
Core

InAsSb 1500 nm

GaInAsSb
Integrated Absorber
1135-nm Total
Thickness

InAs/GaInSb/InAs
5 Type II QWs

Bottom
Cladding

AlAsSb 2000 nm

AlAsSb 500 nm

GaSb 500 nm

AlAsSb 1500 nm

Substrate

GaSb

GaSb
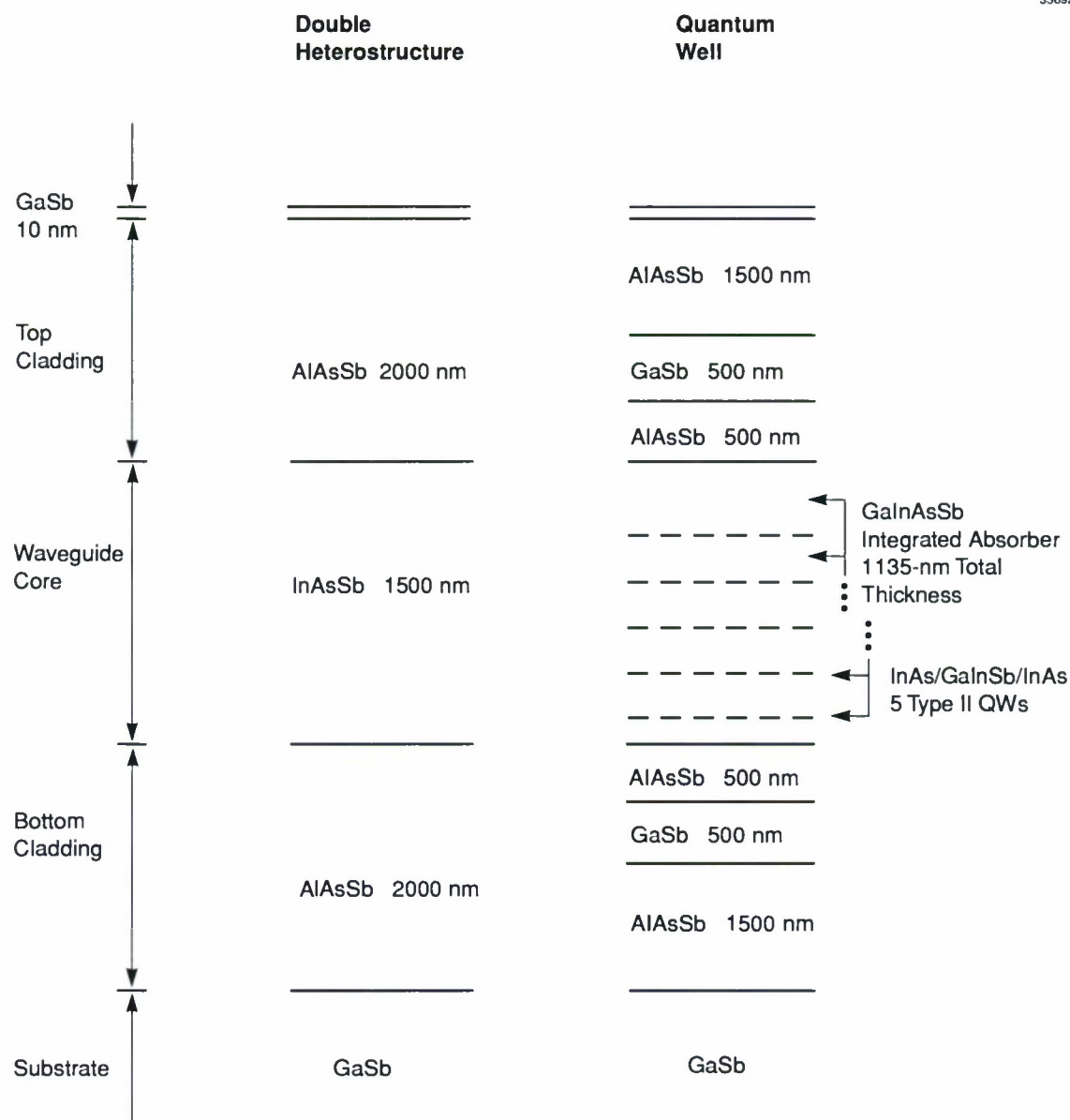
Figure 1-1. Epitaxial layer structure for double-heterostructure (DH) and quantum-well (QW) lasers. Please note that the layers are not drawn to scale.

2
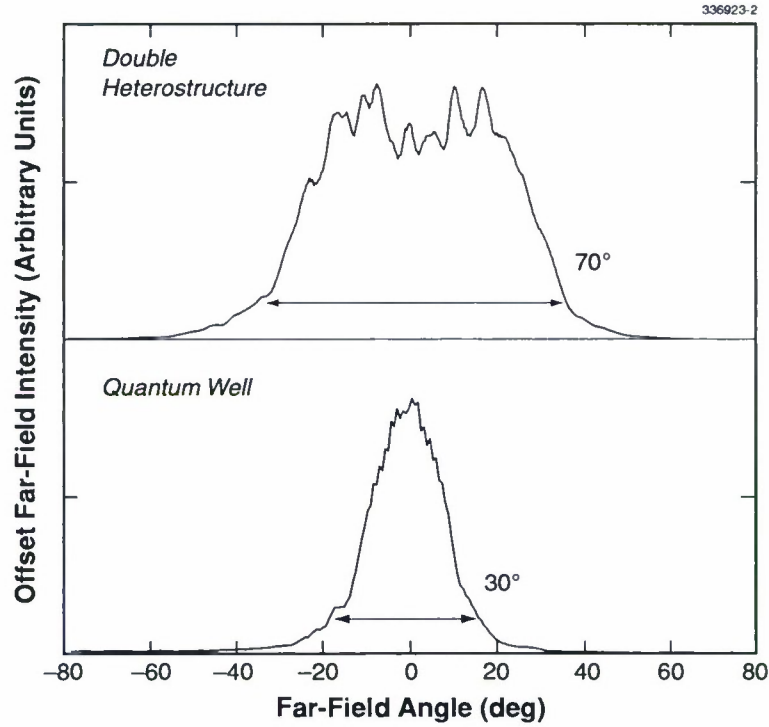
Figure 1-2. Lateral far-field intensity profile of DH and QW lasers. The arrows indicate the full width at $1/e^2$ of the profiles.

After thinning the substrates to ~100-μm thickness and applying an antireflection coating to the substrate (pump) side of the semiconductor chip, 2.2-mm-long devices were mounted active-side down on heatsinks. The front and back facets were then low- and high-reflection coated. The devices werc cooled to 77 K in a liquid nitrogen dewar and pumped using a diode laser array emitting at ~1.85 μm. The pump stripe width was adjusted to get the highest peak power from the devices. For an incident peak pump power of 27 W (100 μs, 2.5% duty cycle), the peak 4-μm power was measured to be 1.6 and 1.9 W for the DH and QW devices, respectively.

The far-field radiation pattern was obtained by placing a paper screen at the dewar window and recording the 4-μm intensity pattern using a Pt:Si focal plane array. Figure 1-2 depicts the far-field intensity pattern in the lateral dimension for both the DH and QW lasers. As can be seen, the divergence angle for thc DH laser is ~2.5× greater than for the QW laser. To determine the laser beam spot size in the lateral dimension, a 0.5-numerical-aperture ZnSe lens was used in conjunction with a Ge camera lens to first image the laser facet onto the Pt:Si focal plane array. Since the beam waist in the lateral dimension is not coincident with thc laser facet, the axial position of the ZnSe lens was then adjusted to obtain a minimum spot size in the lateral dimension. This axial displacement is taken to be the beam astigmatism. For the DH

3
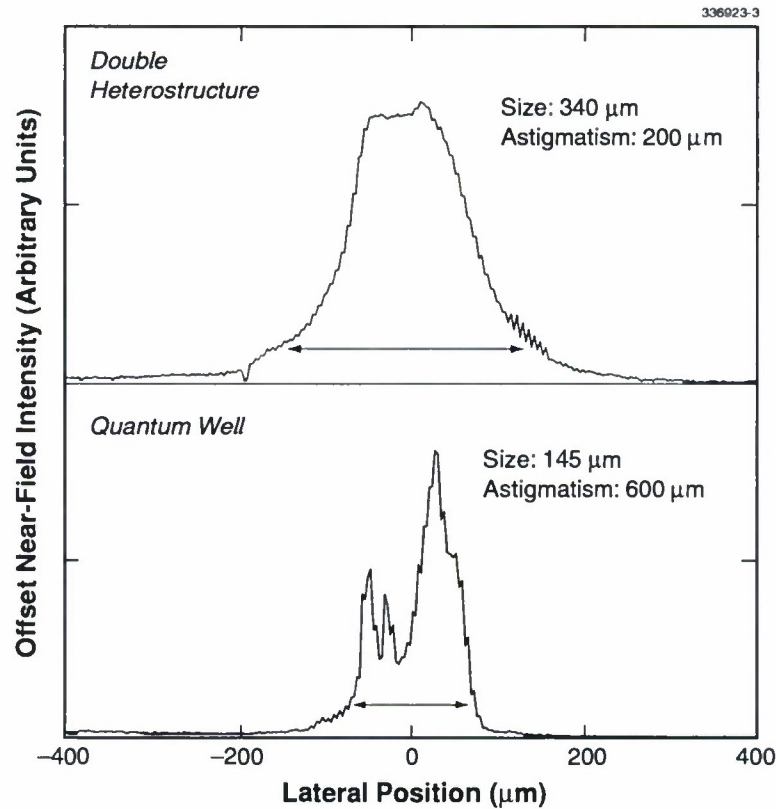
Figure 1-3. Lateral near-field intensity profile of DH and QW lasers at the axial position of minimum spot size. The arrows indicate the full width at $1/e^2$ of the profiles.

device, beam astigmatism was measured to be roughly 200 μm, which corresponds to a beam waist position in the semiconductor chip of ~700 μm from the output facet. For the QW device, the astigmatism was consistently measured to be ~600 μm, which places the beam waist in the semiconductor chip at the high-reflectivity back facet. Such a large astigmatism would be expected in the limit of zero antiguiding. Figure 1-3 depicts the intensity profile of this virtual source within the laser cavity. As can be seen, the spot size for the DH laser is ~2.5x greater than for the QW device. From this data, the etendue (the divergence, spot size product) in the lateral dimension is calculated to be 75 and 425 mm·mrad for the QW and DH laser, respectively. Since the brightness equals the power divided by the etendue, one finds that the brightness of the QW laser is more than 6x greater than that of the DH laser.

A. K. Goyal   P. Foti
H. K. Choi   C. C. Cook
G. W. Turner   B. Lax
A. Sanchez   J. R. Ochoa
S. C. Buchter   S. D. Calawa
M. J. Manfra

4

REFERENCES

1. H. Q. Le, C. H. Lin, and S. S. Pei, *Appl. Phys. Lett.* **72**, 3434 (1998).

2. C. L. Fclix, W. W. Bewley, I. Vurgaftman, L. J. Olafscn, D. W. Stokcs, J. R. Meyer, and M. J. Yang, *Lasers and Electro-Optics Society Annual Meeting* (IEEE, Piscataway, N.J., 1999), Paper WY3.

3. R. Q. Yang, J. D. Bruno, J. L. Bradshaw, J. T. Pham, and D. E. Wortman, *Electron. Lett.* **35**, 1254 (1999).

4. H. Q. Lc, G. W. Turner, and J. R. Ochoa, *IEEE Photon. Technol. Lett.* **10**, 663 (1998).

5. M. Mikulla, P. Chazan, A. Schmitt, S. Morgott, A. Wetzel, M. Walther, R. Kiefer, W. Pletschen, J. Braunstein, and G. Weimann, *IEEE Photon. Technol. Lett.* **10**, 654 (1998).

6. G. Dente, private communication.

2. ELECTRO-OPTICAL MATERIALS AND DEVICES

2.1 THERMOELECTRIC QUANTUM-DOT SUPERLATTICES WITH HIGH ZT

Whall and Parker [1] first suggested using multilayer systems prepared by molecular-beam epitaxy (MBE) for improved thermoelectric materials. Several papers [2] were presented on thermoelectric super-lattices in 1992 including experimental results on PbSeTe/BiSb superlattices by Lincoln Laboratory [3]. Reduced dimensional superlattice systems were proposed as a means to greatly enhance the thermoelectric figure of merit (ZT) as a result of the effects of confinement on the electronic density of states [4]–[6]. Subsequently, it was shown that additional effects need to be included in order to obtain a more complete understanding of these complex structures [7],[8]. Recently, there has been an increasing interest in quantum-well and quantum-wire superlattice structures in the search to find improved thermoelectric materials for applications in cooling and power generation [9]. An earlier experimental investigation of $Pb_{1-x}Eu_xTe/PbTe$ quantum-well superlattices grown by MBE yielded an enhanced ZT due to the quantum confinement of electrons in the well part of the superlattice structure [10],[11]. Quantum wires have been calculated to have much higher ZTs than quantum wells [6]. Quantum dots (QDs) may have even higher ZT values than quantum wires.

Quantum dots represent the ultimate in reduced dimensionality, i.e., zero dimensionality. The energy of an electron confined in a small volume by a potential barrier as in a QD is strongly quantized, i.e., the energy spectrum is discrete. For QDs, the conduction band offset and/or strain between the QD and the surrounding material act as the confining potential. The quantization of energy, or alternatively the reduction of the dimensionality, is directly reflected in the dependence of the density of states on energy. For a zero-dimensional system (QD), the density of states dN/dE of the confined electrons has the shape of a delta-like function [12]

$$dN/dE \propto \sum_{\varepsilon_i} \delta\left(E - \varepsilon_i\right) \quad , \tag{2.1}$$

where e_i are discrete energy levels and δ is the Dirac function. Thus, an enhanced density of states is a possibility even in partially confined QD superlattice (QDSL) structures. Consequently, an enhancement in the Seebeck coefficient S and the thermoelectric power factor $P = S^2\sigma$ (where σ is the electrical conductivity) may occur for a suitable structure in which the chemical potential lies within a few kTs of the delta-like function of the ground state and/or one of the excited states of the partially confined QDs. In addition, the chemical potential should lie near a suitable band edge of a good thermoelectric material. In real materials, tunneling, thermal and inhomogeneous broadening, as well as a weak potential barrier surrounding the QD may contribute to reducing the confinement effect. An enhancement of the Seebeck coefficient and the power factor in the PbSeTe/PbTe QDSL system has been reported [13].

In addition to the possibility of an enhancement in the power factor, another advantage of having a QDSL structure is the enormous density of dissimilar materials interfaces (involving the wetting layer, the matrix or spacer layer, and dot layer of the QDSL structure), which is expected to lower the lattice thermal

conductivity to values below those attainable by merely alloying [14]. Experimental results on the reduction of the thermal conductivity of superlattices have been reported in which the values were much lower than that of their constituents and even smaller than the thermal conductivity value of the equivalent compositional alloys [15]. The possibility of phonon engineering combined with power-factor engineering may result in large improvements in the ZT of already good thermoelectric materials.

A significant lattice mismatch is needed in order for islands or dots to form. A good thermoelectric material is needed in order to start with a reasonably high ZT. It is conjectured that a high static dielectric constant is needed not only to suppress impurity scattering of the electron carriers but also to minimize interface scattering of the carriers. ZT increases as the lattice thermal conductivity decreases for constant temperature, power factor, and electronic part of the total thermal conductivity. Upon considering the above criteria, the PbSeTe/PbTe superlattice system appears to be a very good model system for investigation of thermoelectric QDSL phenomena.

As a first step to realizing large improvements in the ZT of a QDSL thermoelectric material, we report on the growth and characterization of QDSL structures composed of $PbSe_{0.98}Te_{0.02}$ QDs and PbTe matrix layers. Please note that QDs have already been reported for a PbSe deposit on a PbTe surface [16] and for a 60-period PbSe/PbEuTe QDSL structure [17],[18]. The islands or QDs form in order to reduce the large heteroepitaxial free energy component and allow the strain in the $PbSe_{0.98}Te_{0.02}$ to partially relax. The islanding process reduces the interface energy by limiting the contact of the $PbSe_{0.98}Te_{0.02}$ with the PbTe surface upon which it is grown, and allows the $PbSe_{0.98}Te_{0.02}$ free surface to at least partially relax. The strain-induced islanding technique produces the QDs and is called the Stranski-Krastanow epitaxial growth method. When enveloped by PbTe matrix material, these islands may possibly be used to partially confine the electrons in the QDs.

For the experimental realization of a large number of QDs with good quality (high degree of ordering), optimal separational distance, and nearly uniform dot size, we use MBE, which is noted for atom layer–by–atom layer control, reproducibility, and flexibility. Another advantage of MBE-grown Pb-salt structures is that the sticking coefficients of well-known MBE growth chamber contaminants is unusually low [19].

The MBE growth is being carried out in a modified 360-type (T-series) growth chamber with an associated custom-built load-lock chamber as described previously [20]. The effusion cells on the cell flange currently being used for the growth of PbSeTe/PbTe superlattice structures contain PbTe, PbSe, BiSb or Bi_2Te_3, and Te. The MBE substrate holder accommodates BaF_2 substrates with 18×18-mm square shape. A 30-keV reflection high-energy electron diffraction (RHEED) system (used at 12 keV) was employed during film growth to optimize and monitor the deposition. Alternating RHEED streaks and chevron-shaped dots were observed throughout the growth runs of the QDSL structures. Molecular- and atomic-beam fluxes arriving at the substrate location were monitored via the beam-flux ion gauge. The main flux measurement tool was a nude Bayard-Alpert gauge, mounted on the manipulator, so that it could be rotated into the substrate position. In this position, the beams from the individual sources can be monitored and calibrated. Precise run-to-run control of composition requires precise knowledge of the PbTe, PbSe, and Te beam fluxes. The beam flux of the n-type dopant source (BiSb or Bi_2Te_3) was adjusted and

8

monitored by measuring the Hall coefficient of grown films by the van der Pauw method. The typical growth rate was 0.8 to 1.4 μm/h. The carrier concentration of the calibration PbTe and PbSe$_{0.98}$Te$_{0.02}$ growth runs and of the PbSe$_{0.98}$Te$_{0.02}$/PbTe superlattice structures were calculated from the Hall coefficient. For the growth of the PbSe$_{0.98}$Te$_{0.02}$/PbTe superlattice structures, the BiSb or Bi$_2$Te$_3$ and the Te shutters were open during the entire growth run, whereas the PbTe and PbSe shutters were alternately opened and closed. A schematic cross section of a PbSe$_{0.98}$Te$_{0.02}$/PbTe superlattice structure along with the approximately 200-nm-thick Bi-doped PbTe buffer layer and the (111) BaF$_2$ substrate is shown in Figure 2-1. After the growth of a 0.6–0.7-nm-thick wetting layer, PbSe$_{0.98}$Te$_{0.02}$ spontaneously grows in the form of QDs. The PbTe grows to replanarize the surface. This behavior automatically repeats itself for over 600 periods in these test structures.

It is well known that lead chalcogenides can be doped by varying the Pb-to-chalcogenide ratio, but this is not the best way to dope the material. Lead vacancies can dope the material p-type whereas chalcogenide vacancies can dope the material n-type. However, the vacancy dopant mechanism yields maximum carrier concentrations of about 1×10^{18} cm^{-3} in our MBE system using thermally evaporated PbSe$_{0.98}$Te$_{0.02}$ and PbTe material because of the low growth temperature (300 to 330°C, as determined by infrared pyrometry), whereas the optimum carrier concentration for a good Pb-chalcogenide thermoelectric material is 6×10^{18} cm^{-3} or higher at 300 K. Thus, an impurity must be used for doping. Years ago at Lincoln Laboratory, the dopant behavior (carrier type) of eleven impurity elements in bulk PbTe was investigated by the Bridgman growth technique and various post-growth annealing processes [21],[22] and their thermoelectric power factors were determined [23]. It turned out that Bi yielded the highest thermoelectric power factors among the dopants investigated.

The field-emission scanning electron microscope (FE-SEM) image (50,000× magnification) in Figure 2-2 shows the QDs after growth of the 240th PbSe$_{0.98}$Te$_{0.02}$ wetting and dot layer and without the 240th PbTe replanarization layer. The film was rapidly cooled to room temperature to preserve this epitaxial surface structure. The white images are the individual QDs in the planar array. There are approximately 9×10^{10} QDs per cm^2 in this last or surface layer of the superlattice. Atomic-force microscopy images also show that the height-to-base aspect ratio of about 1:3 is much larger than for other materials systems, and their narrow size distribution is much narrower than for the other systems.

The Seebeck coefficient vs carrier concentration is shown in Figure 2-3. Data for the best bulk PbTe, the PbTe/Te superlattice, and the new QDSL structures are given. Our data indicate that the Seebeck coefficient of the best bulk PbSe follows the same curve as the PbTe and may be described by the following empirical Seebeck coefficient S vs carrier concentration n relationship [11]

$$S\,(\mu V/K) = -477 + 175 \log 10\,(n/10^{17}\ \text{cm}^{-3})\ . \tag{2.2}$$

Currently, the most plausible explanation for the Seebeck-coefficient enhancement for the PbTe/Te data shown in Figure 2-3 appears to be that the effective scattering parameter r is increased as a result of extra scattering introduced by the extra Te adsorbed periodically in the PbTe lattice [20],[24]. The increased Seebeck-coefficient enhancement for the QDSL structure is believed a consesequence of quantum effects from

336923-4

PbTe

PbTe Buffer

PbSeTe

BaF$_2$ Substrate
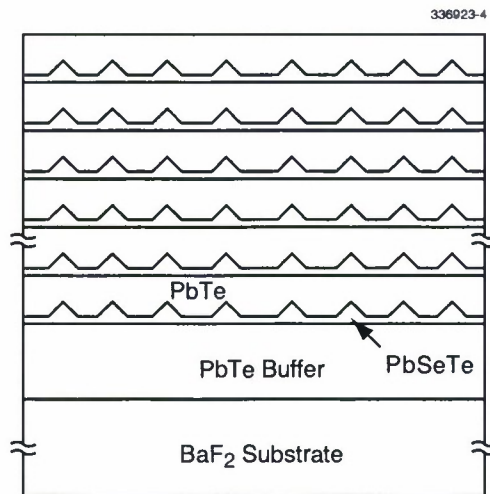
Figure 2-1. Schematic cross section of quantum-dot superlattice structure (QDSL) investigated.

336923-5
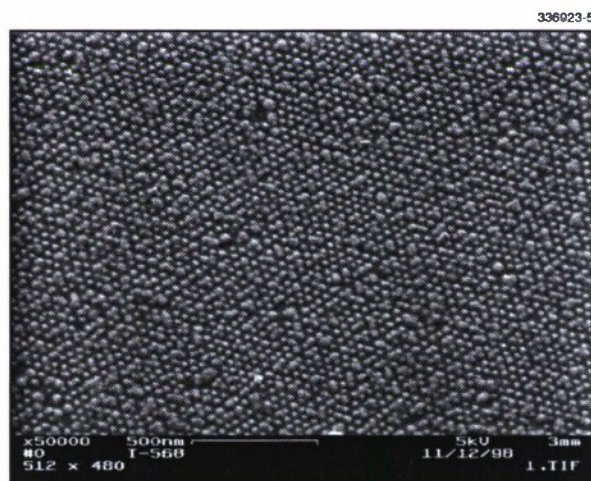
Figure 2-2. Field-emission scanning electron micrograph of QDSL structure.

10
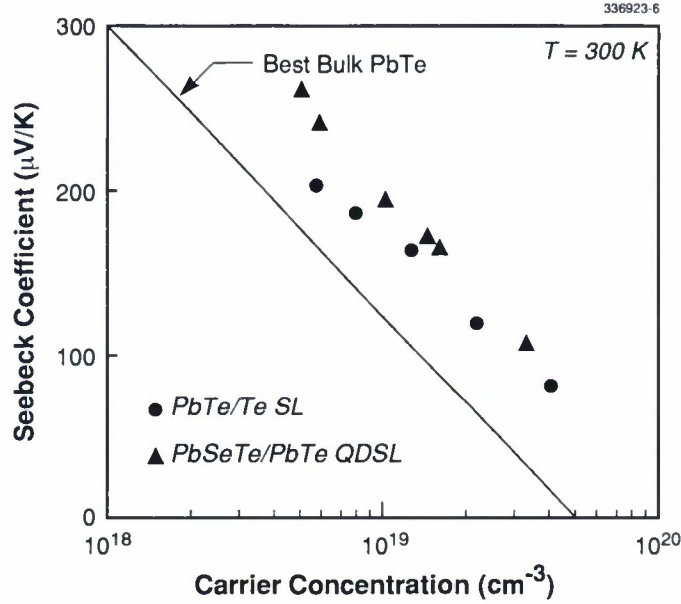
Figure 2-3. Seebeck coefficient vs carrier concentration for n-type PbTe-based structures.

the reduced dimensionality of partially confined electrons in the $PbSe_{0.98}Te_{0.02}$ QDs as well as a more favorable scattering mechanism. The Seebeck coefficients of all $PbSe_{0.98}Te_{0.02}$/PbTe samples in Figure 2-3 are much greater than the values calculated from the S vs n relationship of Equation (2.2).

The thermoelectric figure of merit vs carrier concentration at 300 K is shown in Figure 2-4 for QDSL samples as well as for bulk PbTe. The solid curve for bulk PbTe was obtained from the power factor using thermal conductivity values calculated from the literature lattice thermal conductivity along with the Weidemann-Franz law as described in Ref. 11. The solid curve provides information near the optimum bulk carrier concentration where ZT = 0.45. ZT values for the QDSL samples are much higher (for the same carrier concentration) than either bulk or homogeneous film PbTe or PbTe/Te. These ZT values were obtained from the measured Seebeck coefficient and electrical resistivity values along with calculated thermal conductivity values. The calculated thermal conductivity values are based on the Wiedemann-Franz law and published experimentally derived values of the lattice thermal conductivity κ_L for the mean or equivalent alloy composition of the QDSL samples. It is well known that $PbTe_{0.5}Se_{0.5}$ has a much lower lattice thermal conductivity [25] than either PbTe or PbSe at 300 K by a factor of 2 to 2.5. We determined the equivalent alloy compositions of each sample by two independent methods, i.e., from x-ray diffraction and growth parameters. However, recent experimental results [26] on the lattice thermal conductivity of Si/Ge superlattice structures (a 4.2% lattice-mismatched system) would suggest that the above estimates for the lattice thermal conductivity of $PbSe_xTe_{1-x}$/PbTe (a 5.2% lattice-mismatched system) superlattice
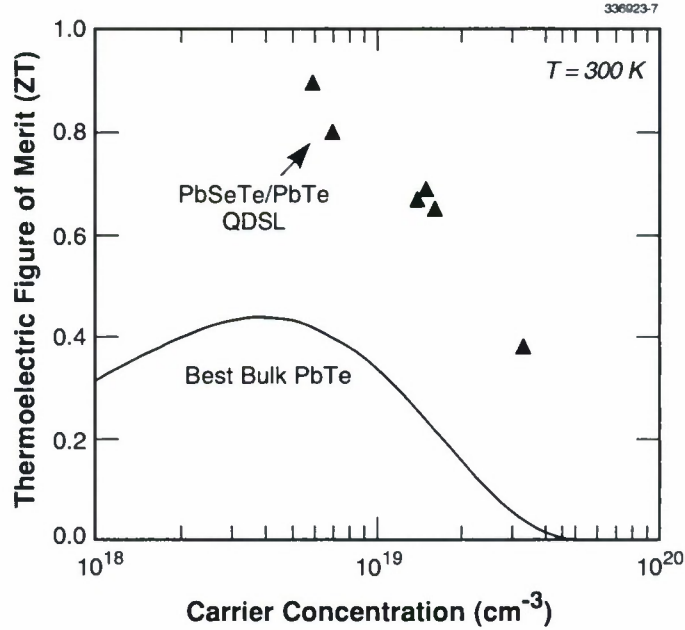
Figure 2-4. Thermoelectric figure of merit vs carrier concentration for bulk PbTe and the new PbSeTe/PbTe QDSL structures.

films are too high. To be conservative, we used the values from Ref. 25 measured on bulk alloys of PbSeTe alloys in our estimates of ZT shown in Figure 2-4. Nevertheless, we found some very high ZTs in these $PbSe_{0.98}Te_{0.02}/PbTe$ superlattice samples of up to about 0.9 at 300 K. Thus, these MBE-grown $PbSe_{0.98}Te_{0.02}/PbTe$ QDSL samples have shown significantly enhanced Seebeck coefficients, power factors, and ZTs.

Large increases in Seebeck coefficient, power factor, and ZT have been measured in PbSeTe/PbTe QDSLs. The improvement in ZT is attributed to the following: (1) a more favorable carrier scattering mechanism due to adsorbed or precipitated extra Te, (2) the presence of $PbSe_{0.98}Te_{0.02}$ islands or dots embedded in a PbTe matrix and believed to result in partial confinement of electrons in the QDs, and (3) the lowering of the lattice thermal conductivity to at least the values of the homogeneous pseudobinary $PbSe_xTe_{1-x}$ alloys. Experimental values for the in-plane room-temperature ZT of Pb-chalcogenide film have been increased from approximately 0.52 for PbTe/Te structures to about 0.9 for $PbSe_{0.98}Te_{0.02}/PbTe$ QDSL structures. Further improvements in the ZT are anticipated based on the potential for lowering the lattice thermal conductivity because of the enormous number of dissimilar materials interfaces present in QDSL structures, and with periods in the 10–15-nm range. Also, many variables need to be optimized including alloying with other compounds.

T. C. Harman P. J. Taylor

D. L. Spears M. P. Walsh

REFERENCES

1. T. E. Whall and E. H. C. Parker, *First European Conference on Thermoelectrics Proceedings* (Pctcr Peregrinus Ltd., London, 1987), p. 51.

2. S. B. Horn, *1st National Thermogenic Cooler Conference Proceedings* (Center for Night Vision and Elcctro-Optics, Fort Belvoir, Va., 1992).

3. T. C. Harman, U.S. Patent No. 5,415,699, issued May 16, 1995; U.S. Patent No. 5,900,071, issued May 4, 1999.

4. L. D. Hicks and M. S. Dresselhaus, *Phys. Rev. B* **47**, 12727 (1993).

5. L. D. Hicks, T. C. Harman, and M. S. Dresselhaus, *Appl. Phys. Lett.* **63**, 3230 (1993).

6. L. D. Hicks and M. S. Dresselhaus, *Phys. Rev. B* **47**, 16631 (1993).

7. J. O. Sofo and G. D. Mahan, *Appl. Phys. Lett.* **65**, 2690 (1994).

8. D. A. Broido and T. L. Reinecke, *Phys. Rev. B* **51**, 13797 (1995); T. L. Reinecke and D. A. Broido, *Proceedings of the XVI International Conference on Thermoelectrics* (IEEE, Piscataway, N.J., 1997), p. 424.

9. G. Mahan, B. Sales, and J. Sharp, *Phys. Today* **50** (3), 42 (1997).

10. L. D. Hicks, T. C. Harman, X. Sun, and M. S. Dresselhaus, *Phys. Rev. B* **52**, R10493 (1996).

11. T. C. Harman, D. L. Spears, and M. J. Manfra, *J. Electron. Mater.* **25**, 1121 (1996).

12. See for example, L. Jacak, P. Hawrylak, and A. Wojs, in *Quantum Dots* (Springer-Verlag, New York, 1998), p. 16.

13. T. C. Harman, P. J. Taylor, M. P. Walsh, and D. L. Spears, presented at 41st Electronic Matcrials Conference, Santa Barbara, Calif., 30 June–2 July 1999; *J. Electron. Mater.* **28** (7), 54 (1999).

14. G. Chen and M. Neagu, *Appl. Phys. Lett.* **71**, 2761 (1997).

15. Sec T. Borca-Tasciuc, D. Song, J. L. Liu, G. Chen, K. L. Wang, X. Sun, M. S. Dresselhaus, T. Radetic, and R. Gronsky, *Thermoelectric Materials 1998*, Vol. 545 of *Materials Research Society Symposium Proceedings* (Materials Research Society, Boston, Mass., 1999), p. 473, and refcrenccs therein.

16. M. Pinczolits, G. Springholz, and G. Bauer, *Appl. Phys. Lett.* **73**, 250 (1998).

17. G. Springholz, V. Holy, M. Pinczolits, and G. Bauer, *Science* **282**, 734 (1998).

18. V. Holy, G. Springholz, M. Pinczolits, and G. Bauer, *Phys. Rev. Lett.* **83**, 356 (1999).

19. N. Frank, A. Voiticek, H. Clemens, A. Holzinger, and G. Bauer, *J. Cryst. Growth* **126**, 293 (1993).

20. T. C. Harman, M. P. Walsh, and D. L. Spears, *J. Electron. Mater. Lett.* **28**, L1 (1999).

21. A. J. Strauss, personal communication.

22. A. J. Strauss, *J. Electron. Mater.* **2**, 553 (1973).

23. T. C. Harman, unpublished material.

24. T. Koga, T. C. Harman, X. Sun, S. B. Cronin, and M. S. Dresselhaus, *Thermoelectric Materials 1998*, Vol. 545 of *Materials Research Society Symposium Proceedings* (Materials Research Society, Boston, Mass., 1999), p. 473, and references therein.

25. E. D. Devyatkova and V. V. Tikhonov, *Sov. Phys. Solid State* **7**, 1427 (1965), and references therein.

26. S. M. Lee, D. G. Cahill, and R. Venkatasubramanian, *Appl. Phys. Lett.* **70**, 2957 (1997).

3. SUBMICROMETER TECHNOLOGY

3.1 MODELING OF DNQ/NOVOLAC RESISTS FOR E-BEAM EXPOSURE

Diazonaphthoquinone (DNQ)/novolac resists were developed for use in i-line photolithography, but these materials also hold great promise for electron-beam lithography in mask making applications. Under a cooperative research and development agreement with SEMATECH and Etec Inc., we have developed techniques to screen DNQ/novolac resists and developers. Our approach involves a combination of modeling, using ProBeam/3D and ProDRM software [1],[2], and patterning verification experiments using e-beam exposure at 50 kV. The modeling software simulates exposure reaction kinetics and dissolution rate effects to calculate the sizing dose and the sensitivity of feature size to dose variations. Seven DNQ/novolac-based resists, which are available commercially from a variety of resist suppliers, were selected as candidates for evaluation as a mask making resist.

The determination of the Dill C parameter, a measure of exposure kinetics, is not readily obtained by traditional uv measurement methods. We have described a new and versatile Fourier transform infrared (FTIR) method to determine the Dill C parameter elsewhere [3] and have employed that method to determine C for all seven resists under evaluation. Values for C measured on chrome on quartz substrates are presented in Table 3-1 both in units of $cm^2/\mu C$, the traditional units associated with the Dill C parameter, and in units of cm^3/J, the latter accounting for the absorbed dose within the resist. Parameter input into ProBeam requires the units to be in the form of cm^3/J, and the conversion factor can be determined via ProBeam simulation.

TABLE 3-1
Dill C Parameters Determined for DNQ/Novolac Resists
Exposed at 50 kV

Manufacturer	Resist	Dill C $(cm^2/\mu C)$	Dill C (cm^3/J)
Clariant	AZ5204	0.0092	0.00133
JSR	IX420H	0.0072	0.00106
Olin	OiR 907-12	0.0073	0.00110
Shipley	SPR700	0.0061	0.00097
Sumitomo	PFM-10A4	0.0070	0.00106
TOK	OEBR2000	0.0079	0.00116
Nippon Zeon	ZMP	0.0070	0.00103

TABLE 3-2
Dissolution Parameters Determined for DNQ/Novolac Resists Exposed at 50 kV and Developed with Aqueous KOH + Ethanol Amine Based Developers

Resist	Developer	R_{max} (nm)	R_{min} (nm)	M_{th}	n	R_0	R_{depth} (nm)
AZ5204	ZMPD	4.04	1.38	0.74	10.95	0.004	111
IX420H	ZT	10.47	0.10	0.67	1.79	0.487	164
OiR 907-12	ZMPD	1.46	0.45	0.68	5.71	0.010	52
SPR700	ZT	11.54	0.06	0.74	1.68	0.114	110
PFM-10A4	ZT	10.02	0.44	0.42	1.26	0.175	95
OEBR2000	ZMPD	2.00	0.28	0.73	3.23	0.010	59
ZMP	ZMPD	56.19	1.11	0.79	1.79	0.057	91

The dissolution rate modeling parameters R_{max} (maximum development rate of fully exposed resist), R_{min} (minimum development rate of unexposed resist), M_{th} (threshold photoactive compound concentration), n (development selectivity), R_0 (relative surface development rate), and R_{depth} (depth for transition from surface to bulk development rate) were determined by measuring resist dissolution rate vs time for multiple resist exposures [4]. These data were analyzed using ProDRM to determine resist development parameters. Each resist was evaluated with up to three different types of developers: an aqueous KOH based developer, an aqueous KOH + ethanol amine based developer, and an aqueous TMAH based developer. The results for aqueous KOH + ethanol amine based developers are listed in Table 3-2.

One difference between e-beam and i-line dissolution parameters is that the R_{max} is exceedingly low for e-beam exposure. Relative to literature values for other developers, R_{max} would be predicted to be almost two orders of magnitude larger. This low value is a direct result of the measurement of R_{max} at only 50% DNQ conversion. At higher exposure doses, where greater amounts of DNQ conversion occur, the resist undergoes apparent crosslinking, and resist development ceases. This behavior is clearly unlike the dissolution behavior observed with i-line exposure and emphasizes the need to determine dissolution parameters with the exposing energy. Finally, the relatively large R_{depth} value and relatively small R_0 value show that the dissolution properties of this resist-developer combination will be strongly influenced by surface inhibition effects.

Electron-beam lithography simulation was performed employing software using the measured modeling parameters described above. A Monte Carlo simulation was performed on a substrate composed of 105 nm of AR3 chrome on silicon dioxide to model electron scattering, followed by running the pixel generation module to account for the 120-nm-diam Gaussian beam shape. The latent image is calculated from

the aerial image and the previously determined Dill C parameter. The final resist linewidth is determined from the latent image and the measured dissolution parameters. The exposure latitude is then calculated based on the variation of linewidth with exposure dose.

Initial resist selection was accomplished by modeling resist linewidth as a function of exposure dose and development time. Simulations were performed on both 600-nm lines in a dense pattern (1:1 pitch) and an isolated 600-nm line (1:3). Resist process modeling was accomplished by determining the expected sizing dose for several development times and using this information to construct a 15- by 15-level designed experiment in which exposure dose and development time are varied for both dense and isolated 600-nm lines. All 450 possible combinations are modeled ($15 \times 15 \times 2$) and the resulting resist linewidths are calculated. A model describing the variation of linewidth as a function of exposure dose and development time can be constructed and an example of such a model for SPR700 with ZT developer is presented in Figure 3-1. From this linewidth information, the dose to size and exposure latitude for dense and isolated lines can be calculated.

The selection criteria for the verification experiments were that the modeled resist will have a dose to size of less than 40 $\mu C/cm^2$ and a $\Delta CD/\Delta\%$ dose of less than 10 nm. All 16 resist-developer pairs in which dissolution parameters were available had their performance modeled, and the six resist-developer pairs which met the above criteria for at least one feature type were selected for lithographic verifications. Table 3-3 summarizes the status of the 21 initial resist-developer pairs showing the six resists that were modeled and selected for lithographic verification and the ten resists in which modeling results suggested that performance would not meet the selection criteria. The five resist-developer pairs in which dissolution parameters were not available are also shown.

It is interesting to note that five of the six resist-developer pairs selected for verification experiments employed a KOH + ethanol amine developer, implying that this developer system may have an advantage over others in e-beam lithography and suggesting that future work should concentrate on developers of this category.

A summary of the measured dose to size and exposure latitude for 600-nm dense and isolated lines exposed at 50 kV from the verification lithography is shown in Table 3-4. All measured results presented meet the selection criteria of sensitivity with the dose less than 40 $\mu C/cm^2$ and of exposure latitude with the $\Delta CD/\Delta\%$ dose less than 10 nm for 600-nm dense and isolated lines. Also shown in Table 3-4 is the modeled resist performance at the process conditions. The modeled performance typically agrees very well with the measured performance and shows the validity of our approach of combining modeled performance with selected lithographic verification.

T. H. Fedynyshyn   W. F. DiNatale
S. P. Doran   D. Lennon
M. L. Lind   T. M. Lyszczarz
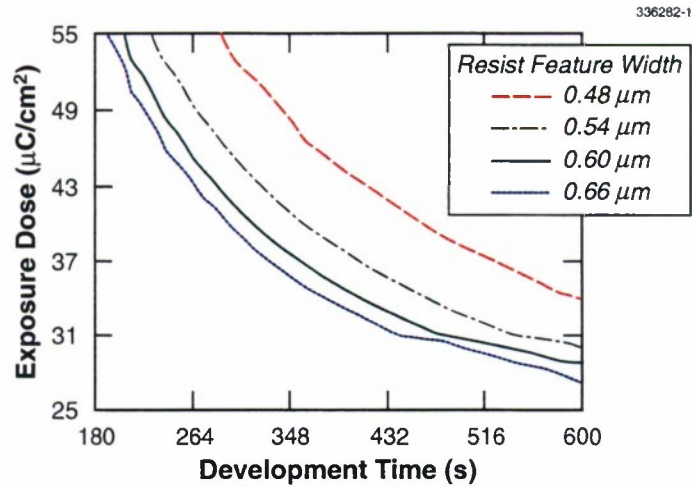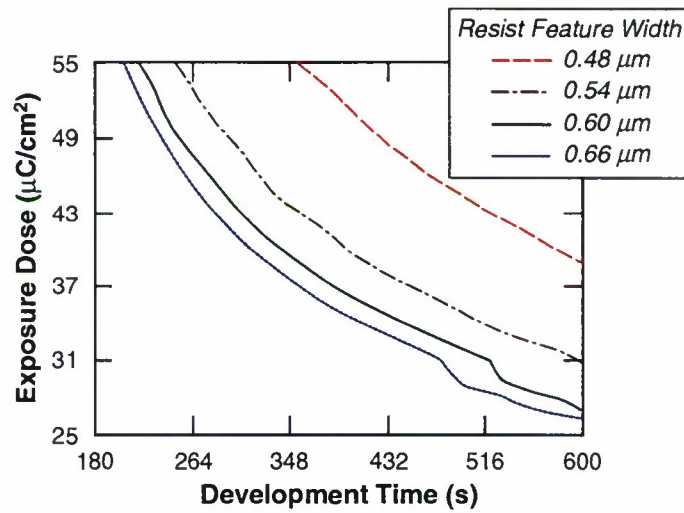
Figure 3-1. ProBeam simulation of 600-nm (a) dense and (b) isolated linewidths as a function of develop time and exposure dose for SPR700 resist with ZT developer.

18

TABLE 3-3
**Summary of Modeled Performance and Selection of Resist
for Verification Trials**

Resist	2.38% TMAH	KOH + Amine	KOH
SPR700	Not Available	Verification	Not Available
IX420H	Modeled	Verification	Not Available
PFM-10A4	Not Available	Modeled	Not Available
ZMP	Modeled	Verification	Verification
AZ5204	Modeled	Modeled	Modeled
OBER2000	Modeled	Verification	Modeled
OiR 907-12	Modeled	Verification	Modeled

TABLE 3-4
Summary of Experimentally Determined and Modeled Values of Dose to Size and of Exposure Latitude for 600-nm Dense and Isolated Lines Exposed at 50 kV

Resist Developer	Develop Time (s)		Dense		Isolated	
			E_{size} ($\mu C/cm^2$)	$\Delta CD/$ $\Delta\%$ Dose (nm)	E_{size} ($\mu C/cm^2$)	$\Delta CD/$ $\Delta\%$ Dose (nm)
ZMP-NZPD	100	Measured	21.3	5.1	21.2	5.4
		Modeled	19.2	8.8	17.7	9.7
ZMP-NZPD	60	Measured	35.5	7.3	34.0	8.2
		Modeled	28.6	8.6	26.3	9.2
SPR700-ZT	50	Measured	17.8	9.1	16.6	16.2
		Modeled	21.7	8.7	20.0	9.4
SPR700-ZT	550	Measured	21.9	5.4	20.3	8.9
		Modeled	24.5	8.6	22.5	9.3
IX420H-ZT	500	Measured	31.2	8.2	27.8	8.2
		Modeled	26.9	6.8	24.7	7.8
IX420H-ZT	400	Measured	40.0	5.3	36.8	6.5
		Modeled	31.5	7.1	29.0	7.7
PFM10A4-ZT	450	Measured	21.0	6.0	19.4	4.8
		Modeled	21.9	6.4	20.2	7.0
PFM10A4-ZT	360	Measured	33.7	9.4	32.3	10.1
		Modeled	28.6	6.6	26.6	7.2
ZMP-MP452	400	Measured	29.0	3.0	28.5	4.1
		Modeled	33.0	17.0	31.1	17.4
ZMP-MP452	270	Measured	43.5	5.8	43.7	7.7
		Modeled	37.7	14.1	35.5	14.7
OiR 907-ZMPD	390	Measured	17.6	3.0	18.9	4.2
		Modeled	24.0	8.5	22.7	8.7
OiR 907-ZMPD	300	Measured	30.2	4.8	28.2	5.5
		Modeled	31.0	8.4	31.1	8.7

3.2 ION MOBILITY SPECTROSCOPY USING LASER IONIZATION

Trace vapor detectors based on chemical-ionization ion mobility spectroscopy (IMS) are a widely used commercially available means for contraband detection. These systems typically use indiscriminate ionization sources such as a radioactive beta emitter or a corona discharge [5] to ionize the ambient nitrogen and/or oxygen, which then initiates a charge cascade through a dopant gas resulting in proton attachment to the target analyte. Here, we report on a technique that uses multiphoton uv laser ionization combined with a conventional IMS detector to achieve superior discrimination against certain interfering compounds such as amines, pyrroles, pyridines, pyrazines, and purines (common interferants when detecting narcotics onboard ships, due to marine oil).

The ionization is carried out using a novel uv microchip laser operating at 266 nm and delivering peak power densities in excess of 50 MW/cm^2. No focusing optics are needed to achieve these power densities. The target compounds themselves, although readily ionized by the radiation, are more efficiently ionized by addition of a reactive gas G at a higher concentration. Laser ionization of the reactive gas G forms the odd-electron radical cation $G\bullet^+$. This radical cation $G\bullet^+$ will collisionally induce ionization in those compounds possessing an ionization potential lower than its own [6],[7]. This method of electron-transfer-mediated chemical ionization has been reported to give mass spectra cracking patterns that depend on the exothermicity of the charge-exchange reaction [8], and hence can be manipulated by choice of reagent.

The experiments were performed using a modified ion mobility spectrometer [9] manufactured by Ion Track Instruments, Inc. The electrodes, voltages, and preamp were not modified, but the ^{63}Ni ionizer was removed and replaced with coplanar 266-nm dielectric mirrors spaced 1 cm apart. A stainless steel grid was placed between the mirrors and suspended ~5 mm away from the entrance to the drift region, thus providing the means to inject the ions into the drift region. An aluminum box surrounded the mirror/grid assembly and was attached via a 0.125-in.-OD fused-silica-lined tube to a gas chromatograph (GC) injector. The mirrors, IMS, and aluminum box were all placed in a temperature-controlled oven. The GC injector was equipped with a carrier gas line to allow for introduction of the laser-chemical ionization agent. A small hole in the aluminum box allowed entry of the laser beam. No attempts were made to filter the 532-nm second-harmonic radiation from the frequency-quadrupled 266-nm radiation. Table 3-5 describes the operational performance of the microchip laser [10] used in our prototype detector.

Prior to demonstrations of multiphoton laser ionization–chemical ionization (MPI-CI), we determined the drift times for various molecular weight species using direct ionization by the laser. Since this method of ionization is known to result in little fragmentation [11], we felt this was the best way to calibrate the modified instrument. Figure 3-2 shows the drift time as a function of parent molecule molecular weight for a variety of species at an oven temperature of ~180°C. The calculated reduced mobilities agree well with published values [12]–[14], and this information was used to assist in initial interpretation of the more complex MPI-CI spectra.

21

TABLE 3-5
Performance Specifications of the Microchip Laser
Used for Photoionization

Wavelength	266 nm
Pulse energy	12 μJ
Pulse duration	270 ps
Peak power	44 kW
Maximum repetition rate	5 kHz
Beam diameter	0.2 mm
Peak power density	>50 MW/cm^2
Power supply	<5 lb

336282-2
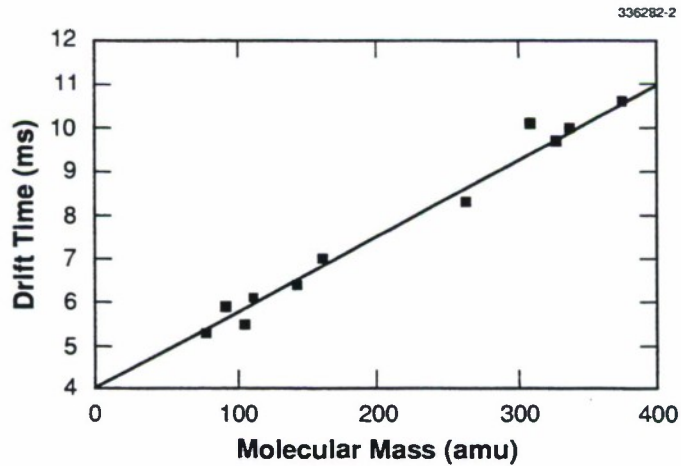
Figure 3-2. Drift time calibration for a number of different compounds measured via direct multiphoton ionization ion mobility spectrometry.

For MPI-CI to work with maximum selectivity, the CI reagent must have an ionization potential higher than the target compound, but lower than many of the common interferants. Aniline (phenylamine) fits this description well. Figures 3-3 and 3-4 show cocaine spectra in the presence of laser ionized aniline for three different counter flows. The injected quantities of cocaine were in the range 0.5–10 ng and are indicated on the Figures. Note the effect the counter flow has on the concentration of aniline dimers. This is thought to be a result of an increased interaction of neutral aniline molecules with ionized aniline in the drift region, as it has been previously reported that such interactions in benzene result in dimerization [15]. We are still investigating the effects of dopant gas concentration and counter-flow rate on the magnitude of competing ionization mechanisms. Under conditions of very high dopant gas concentration and zero counter flow we may begin to see some collisional ionization occurring via proton attachment in addition to electron transfer. In order to determine the role proton attachment may be having in ionization, we injected a sample of cocaine in a methanol/water solution and saw no change in the signal and no low-mass ions formed. Based on this observation, we believe the predominant ionization mechanism to be electron transfer.

We also determined the detection limits of our prototype system under the most sensitive conditions of no counter flow. Figure 3-5 shows the signal as a function of the mass of cocaine injected for two reactive gas intermediates, xylene (a mixture of ortho, meta, and para) and aniline. From this, we see a minimum detectable quantity of ~50 pg and usable signals at ~200 pg. The detection limits with the counter flow are somewhat less because in this prototype the counter flow tends to push the aniline and cocaine away from the laser beam, which is propagating in a sheet ~2 mm above the entrance grid to the drift region.

In addition to detection of pure cocaine, we have tested our MPI-CI detection scheme with other compounds. Table 3-6 provides a list of compounds we've tested. We have not yet quantified the response functions of all these compounds. Results of such tests, when obtained, will indicate the relative rate constants for the charge exchange reactions in these compounds.

R. R. Kunz
J. J. Zayhowski

Aniline Dimer

Aniline | |Cocaine

Signal (Arb. Units)

Aniline Only

Aniline + 0.5 ng Cocaine

Aniline + 2 ng Cocaine

0   5   10   15   20

Drift Time (ms)
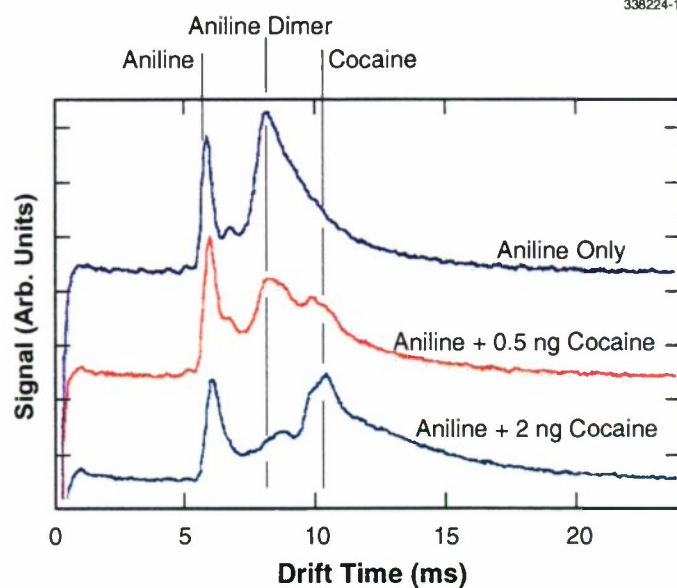
Figure 3-3. Cocaine spectra in the presence of laser ionized aniline. The aniline was present at ~1 ppm, the counter flow was ~100 sccm, and the carrier gas was nitrogen.

Aniline Dimer

Aniline | | Cocaine

Signal (Arb. Units)

Aniline Only

Aniline + 5 ng Cocaine

Aniline + 10 ng Cocaine

0   5   10   15   20

Drift Time (ms)
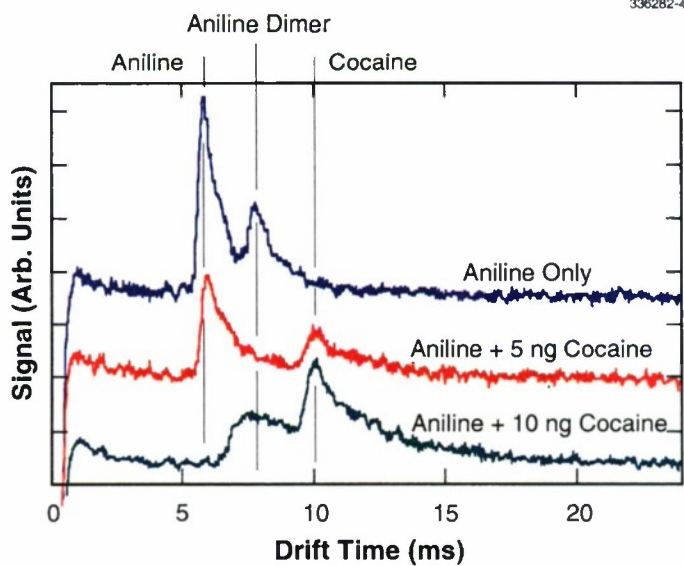
Figure 3-4. Cocaine spectra in the presence of laser ionized aniline. The aniline was present at ~1 ppm, the counter flow was ~50 sccm, and the carrier gas was nitrogen.

24
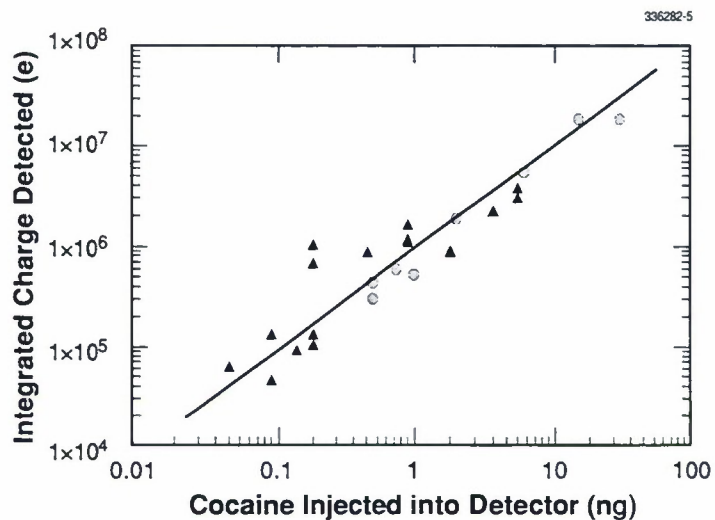
Figure 3-5. Sensitivity curve for detection of cocaine in the presence of laser ionized aniline (triangles) and laser ionized xylene (circles). The counter flow was zero, and the carrier gas was nitrogen.

TABLE 3-6
List of Compounds Tested Using Aniline as a Carrier Gas*

Detected	Not Detected or Weak Response
Lysergic acid diethylamide	Benzene
Heroin	N-methyl pyrrolidone
Caffeine	Toluene
Nicotine	Methanol
Naphthalene	Isopropanol
Ethylene diamine	Cyclohexane
	Xylene
	Water

*The relative responses for these compounds have not yet been quantified. Please note that the selectivity of this detection method is greatly influenced by the reactive gas used (in this case aniline), and vastly different results might be expected for other reactants.

REFERENCES

1. C. A. Mack, *Proc. SPIE* **3048**, 76 (1997).

2. C. A. Mack, *Proc. SPIE* **3236**, 216 (1997).

3. T. H. Fedynyshyn, S. P. Doran, and C. A. Mack, *Proc. SPIE* **3678**, 1263 (1999).

4. T. H. Fedynyshyn, S. P. Doran, M. L. Lind, T. M. Lyszczarz, W. F. DiNatale, D. Lennon, C. Sauer, and J. Meute, *Proc. SPIE* **3678**, 1273 (1999).

5. G. A. Eiceman, *Int. J. Environ. Anal. Chem.* **33**, 161 (1988).

6. A. G. Harrison, *Chemical Ionization Mass Spectrometry* (CRC Press, Boca Raton, Fla., 1992), p. 12.

7. W. J. Simonsick, Jr. and R. A. Hites, *Anal. Chem.* **58**, 2114 (1986).

8. J. A. Herman, Y.-H. Li, and A. G. Harrison, *Org. Mass. Spectrom.* **17**, 143 (1982).

9. P. Becotte-Haigh, A. Maines, and W. McGann, presented at the 6th International Conference on Ion Mobility Spectrometry, August 1997.

10. J. J. Zayhowski and C. Dill III, *Opt. Lett.* **19**, 1427 (1994); J. J. Zayhowski, U.S. Patent No. 5394413.

11. D. M. Lubman and M. N. Kronick, *Anal. Chem.* **55**, 1486 (1983).

12. W. McGann, A. Jenkins, K. Ribiero, and J. Napoli, *Proc. SPIE* **2092**, 64 (1993).

13. L. Kolaitis and D. M. Lubman, *Anal. Chem.* **58**, 1993 (1986).

14. J. W. Leonhardt, H. Bensch, D. Berger, M. Nolting, and J. I. Baumbach, *Proceedings of the Third International Workshop on Ion Mobility Spectrometry* (Lyndon B. Johnson Space Center, Houston, 1995), p. 49.

15. F. H. Field, P. Hamlet, and W. F. Libby, *J. Am. Chem. Soc.* **89**, 6035 (1967).

4. BIOSENSOR AND MOLECULAR TECHNOLOGIES

4.1 "MAGIC" SENSOR FOR BIOLOGICAL AND CHEMICAL SUBSTANCES

A new bioelectronic sensor called MAGIC (Membranes with Antigen-Gated Ion Channels) is being developed that is designed to detect and identify a wide range of biological and chemical substances. As implied by its name, the sensor uses bilayer membranes with ion channels that open to create a measurable electrical current flow when they detect specific substances of interest such as antigens. Potential applications for this sensor include identifying pathogenic organisms or molecules for medical diagnostics or biological/chemical agent detection; analyzing or sequencing DNA or RNA; monitoring the quality of water, food, air, etc.; detecting drugs, explosives, or other chemicals; and screening for or monitoring diseases such as cancer.

The basic principles of this sensor design are depicted in Figure 4-1. A MAGIC sensor would have lipid bilayers containing antigen-gated ion channels, which would consist of ion channel proteins coupled to recognition molecules specific for certain substances. Depending on the substances to be detected, the recognition molecules could be antibodies, oligonucleotides, or other molecules. Binding of an analyte of interest to an appropriate recognition molecule would open the ion channel to which that recognition molecule is coupled, creating an ionic current flow that could be detected via adjacent electrodes. This approach could be implemented in a microfluidic chip, which could contain many different sectors of
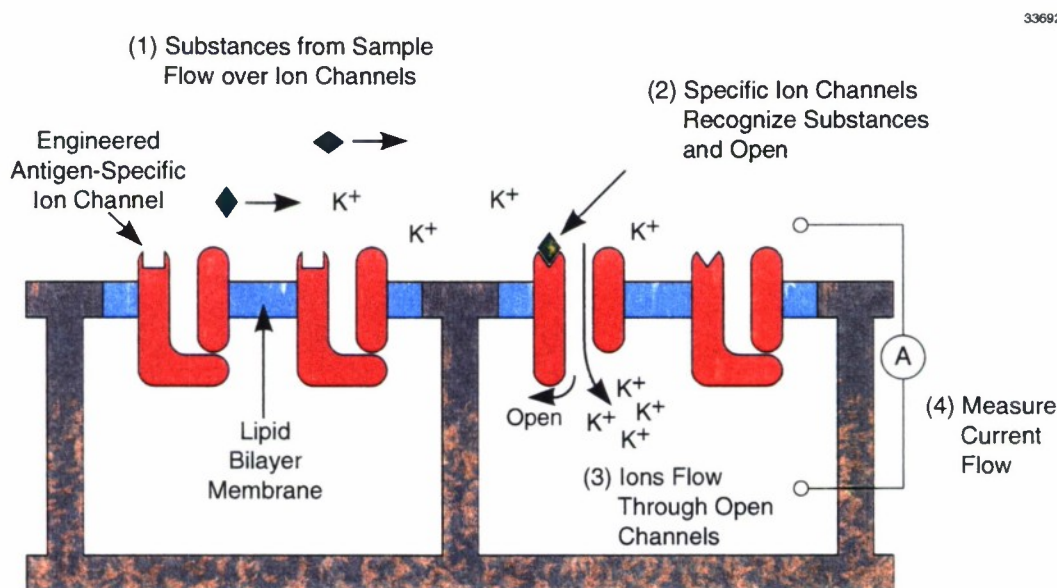
Figure 4-1. Fundamental principles of MAGIC sensor.

27

membranes and ion channels, where each sector would have recognition molecules specific for a different substance. Fluid containing samples taken from blood, air, or other sources could be flowed over the membranes in the microfluidic chip to test for the presence of substances of interest.

Key advantages of the MAGIC sensor design include (1) the ability to accurately identify a very wide range of substances, including specific DNA or RNA sequences, chemicals, toxins, bacteria, and viruses; (2) a standardized and straightforward method of redesigning the specificity of the ion channels once prototype channels have been engineered; (3) a response time of <1 s (for comparison, even the fastest polymerase-chain-reaction-based DNA detection takes ~7 min); (4) potential single-molecule sensitivity (a single molecule could open an antigen-gated ion channel, which would generate a measurable electrical signal); and (5) a simple and robust nonliving approach.

The simplest way to create antigen-gated ion channels is to utilize mechanosensitive ion channels that open in response to physical stretching or pulling on the ion channel proteins. A well-characterized example of such a channel is the mechanosensitive channel of large conductance (MscL) from the bacterium *Escherichia coli* [1]. The ability to detect specific substances would be introduced by attaching a recognition molecule either to MscL itself or to the membrane containing MscL, as shown in Figure 4-2. Binding of a substance to the recognition molecule would apply force to the mechanosensitive ion channel or the surrounding membrane, open the channel, and generate a detectable electrical signal. To facilitate opening of the ion channel, one could utilize previously identified MscL mutants that require very low forces to open [2] or externally apply force to the substance to be recognized via electrophoresis, fluid flow, magnetic beads, or other methods. For simplicity, antigen-coated magnetic beads are used in our preliminary experiments.
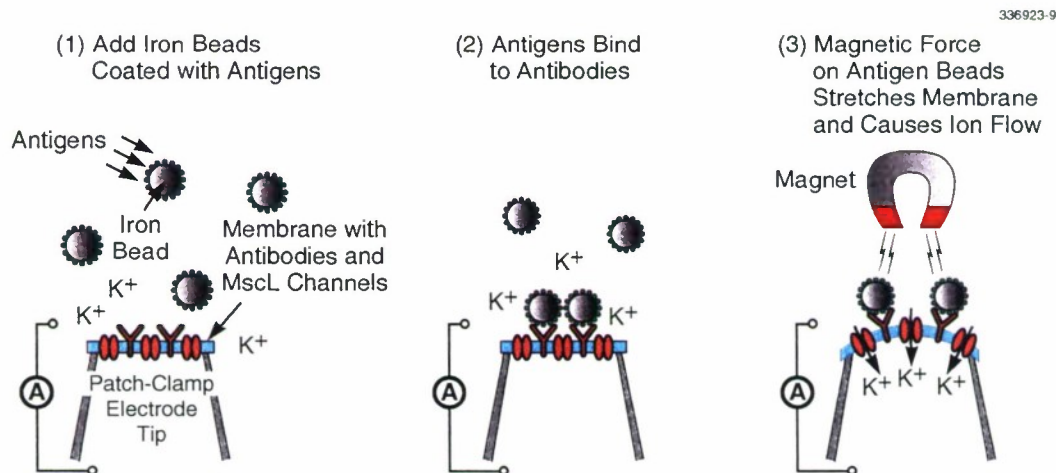
Figure 4-2. Simple MAGIC sensor using the MscL mechanosensitive ion channel.
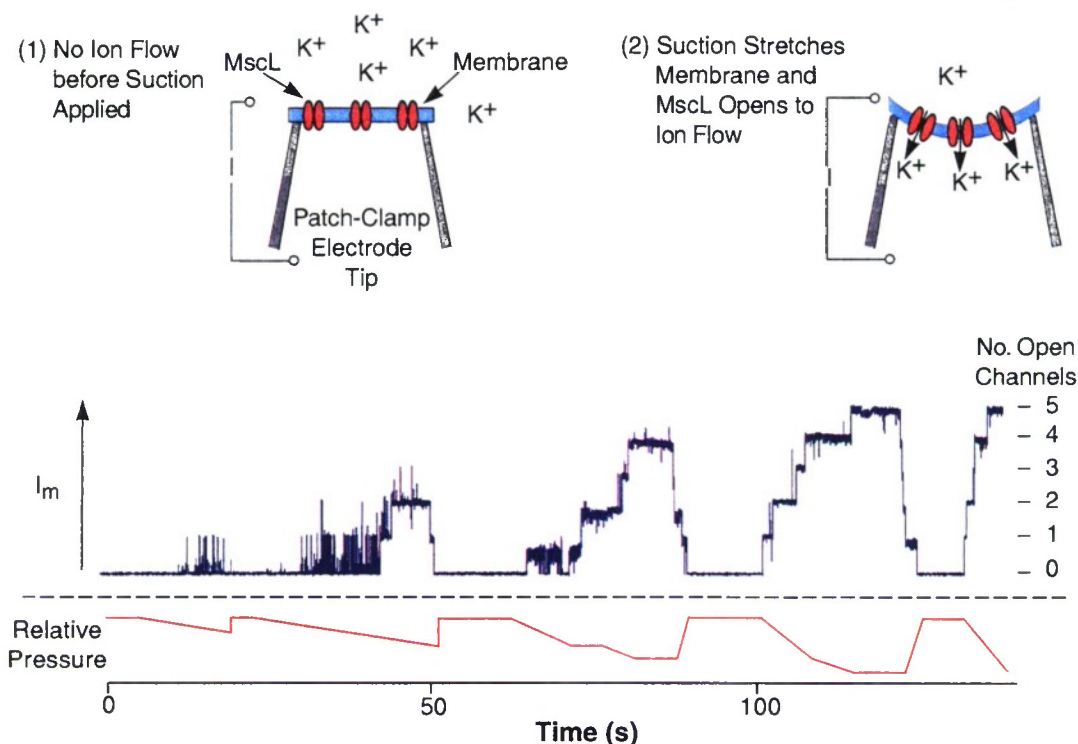
Figure 4-3. Preliminary results from experiments with MscL ion channels.

In order to demonstrate the feasibility of this concept, we have purifed the MscL ion channel from *E. coli* and reconstituted it into artificial lipid membranes. As shown in Figure 4-3, these membranes were positioned on the tip of a patch-clamp pipette electrode so that the current flowing through the ion channels could be measured. Applying suction through the pipette stretched the membrane and pulled the ion channels open, creating an electrical current flow through the channels. As shown in Figure 4-3, this technique was so sensitive that individual ion channels could be counted as they opened up and added to the current flow. Experiments are now under way to link antibodies to these membranes in order to create a simple antigen-sensitive detector like that shown in Figure 4-2.

There is a second and more sophisticated method of creating antigen-gated ion channels which can be explored in the future. This method would employ modified ligand-gated ion channels that open when they bind a specific ligand. A particularly promising candidate is the cyclic-GMP-gated ion channel. This channel has a well-characterized ligand-binding region and has already been modified to alter ligand specificity using both site-directed mutagenesis [3] and chimeric binding-domain replacement [4]. To create sensors utilizing this channel, one could use a similar approach to create chimeric channels with the

29
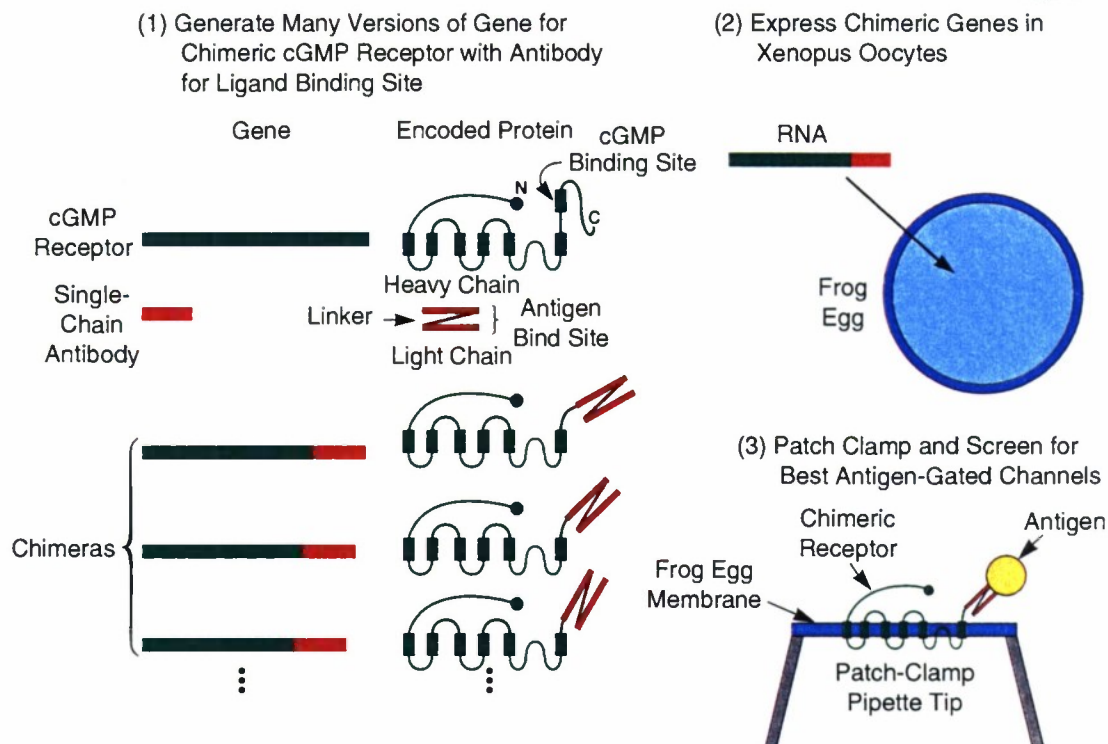
Figure 4-4. Method of engineering ligand-gated channels for MAGIC sensors.

cGMP-binding region of the ion channel replaced by an appropriate recognition molecule such as a single-chain antibody or a DNA-binding domain, as shown in Figure 4-4. Genes for the chimeric channels could be expressed in *Xenopus* oocytes and screened using standard patch-clamp techniques to identify those with the best antigen-gating properties.

In summary, we are developing a new bioelectronic sensor for detecting a wide variety of chemical and biological substances. The sensor uses membranes with antigen-gated ion channels and should be extremely fast, sensitive, and versatile, with applications ranging from biological and chemical warfare agent detection to DNA analysis. We are currently conducting experiments to demonstrate the feasibility of this basic concept by engineering and testing prototype antigen-gated ion channels.

T. H. Rider

J. D. Harper

REFERENCES

1. S. I. Sukharev, P. Blount, B. Martinac, and C. Kung, *Annu. Rev. Physiol.* **59**, 633 (1997).

2. X. Ou, P. Blount, R. J. Hoffman, and C. Kung, *Proc. Natl. Acad. Sci. USA* **95**, 11471 (1998).

3. M. D. Varnum, K. D. Black, and W. N. Zagotta, *Neuron* **15**, 619 (1995).

4. E. H. Goulding, G. R. Tibbs, and S. A. Siegelbaum, *Nature* **372**, 369 (1994).

5. ADVANCED IMAGING TECHNOLOGY

5.1   NOISE INVESTIGATION OF *n*-TYPE BURIED CHANNEL MOSFETs

Most scientific charge-coupled device (CCD) imagers use buried channel transistors in a source follower configuration to convert charge packets into a usable output voltage. The buried channel transistors have relatively low $1/f$ noise which is important for good signal-to-noise ratios at low signal levels. Unfortunately, the $1/f$ noise presently limits the detection of very small charge packets created in the CCD imager. This report describes an investigation of $1/f$ amplitude and phase noise for the *n*-type buried channel transistors. The important result from the investigation is a correlation that exists between measured $1/f$ amplitude and phase noise. The correlation is qualitatively expected since small amplitude fluctuations can be shown to be linearly related to small transit time fluctuations (phase fluctuations) [1] for the buried channel transistor. (The analysis in Ref. 1 is for a bipolar transistor but a similar analysis can be done for the metal oxide semiconductor field-effect transistor MOSFET.) The relationship between the amplitude and phase noise may be important in future readout amplifier designs for reducing $1/f$ noise.

Shown in Figure 5-1 is a schematic of the experimental setup used to make the noise measurements. To measure the $1/f$ amplitude noise, the source follower output signal, after going through a low-pass filter (3-dB frequency is 2 MHz), is sent directly to a fast Fourier transform (FFT) analyzer. The phase noise is measured by passing a small signal (10.7 MHz) through the source follower and a band-pass filter (10.7-MHz center frequency and 3-dB bandwidth frequencies at 8.9 and 12.7 MHz) and then comparing this signal to a reference signal (10.7 MHz) using a phase detector. The output voltage of the phase detector, which is proportional to the phase noise ϕ (phase detector output = $A \sin \phi \approx A\phi$ for small signals) of the source follower amplifier, is also input to the FFT analyzer.

Figure 5-2 is a plot of coherence (defined as $E(XY)/[E(X^2)E(Y^2)]^{1/2}$, where E denotes expectation value and X and Y are random variables with zero mean) vs the logarithm of the frequency for the $1/f$ amplitude and phase noise. The plot shows that the $1/f$ amplitude and phase noise are strongly correlated over the frequency range where the $1/f$ noise dominates the thermal noise. The correlation decreases as the thermal noise becomes more significant at higher frequencies. A qualitative explanation for the correlation is that the $1/f$ amplitude noise and the transistor transit time are both proportional to the mobility [2], resulting in the $1/f$ noise fluctuations being correlated to the upconverted phase noise.

The correlated phase noise can be subtracted from the $1/f$ amplitude noise to reduce the total noise. To determine the improvement in signal-to-noise ratio by doing the subtraction, the change in the signal caused by the subtraction must also be investigated. To evaluate the change, a low frequency signal (10 kHz) was sent through the source follower to compare the signal-to-noise at the output of both the source follower and phase detector. The high frequency 10.7-MHz signal was still used to measure phase shifts. The low frequency amplitude modulation at the gate of the source follower modulates the transit time (phase) of the high frequency signal. A 10-kHz signal is observed at the output of the phase detector due to

10.7-MHz Video
Osc. 10-kHz
Osc.

10.7 MHz

Power Divider

HPF

Phase Shifter

10.7 MHz + Phase Noise + 10-kHz Video Phase Shift

BPF 10.7 MHz

A_G

Limiter

10-kHz Video Amplitude + Amplitude Noise

R_L

LPF 3 dB, 2 MHz

A_G

Phase Detector

Signal Analyzer

Phase Noise and and Video Phase Shift Converted to an Amplitude
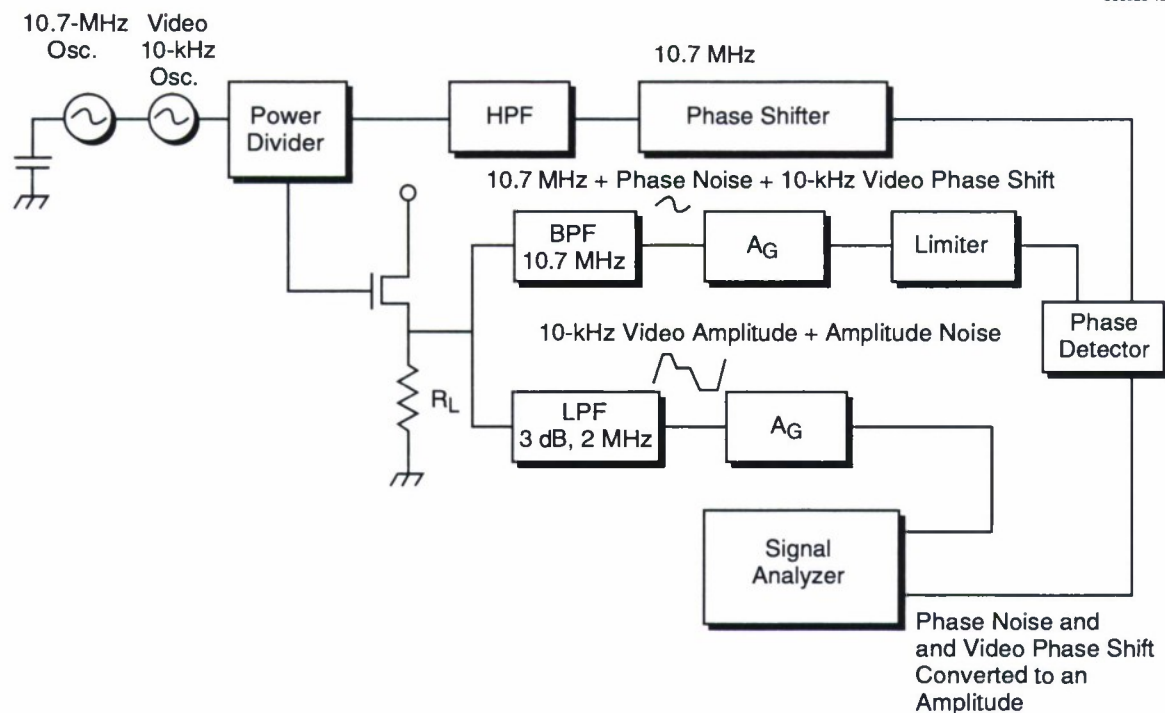
Figure 5-1. Schematic diagram of experimental setup used to measure 1/f amplitude and phase noise as well as determine the correlation for n-type buried channel transistors.

the transit time modulation. Figure 5-3 is a graph of the power spectral density vs frequency. The data displayed for the phase detector output has been multiplied by a constant so the signal peaks of the source follower and phase detector are equal at 10 kHz. After scaling, the power spectral density curve, which shows both 1/f noise and 10-kHz signal, is essentially the same at the output of the source follower and phase detector, indicating that the signal-to-noise ratio is the same. The fact that the two curves are the same argues that the phase detector output cannot be used to reduce the 1/f amplitude noise without reducing the signal by a similar amount.

The 1/f amplitude originates in the channel of the MOSFET while the input signal is applied to the gate. Because of this difference, proper design of the MOSFET should cause the phase shift dependence on the 1/f amplitude noise to be different from that caused by the signal. Future work will investigate if this difference in phase shift dependence exists and can be exploited.

G. J. Coram*
R. K. Reich

*Author not at Lincoln Laboratory.

336923-13
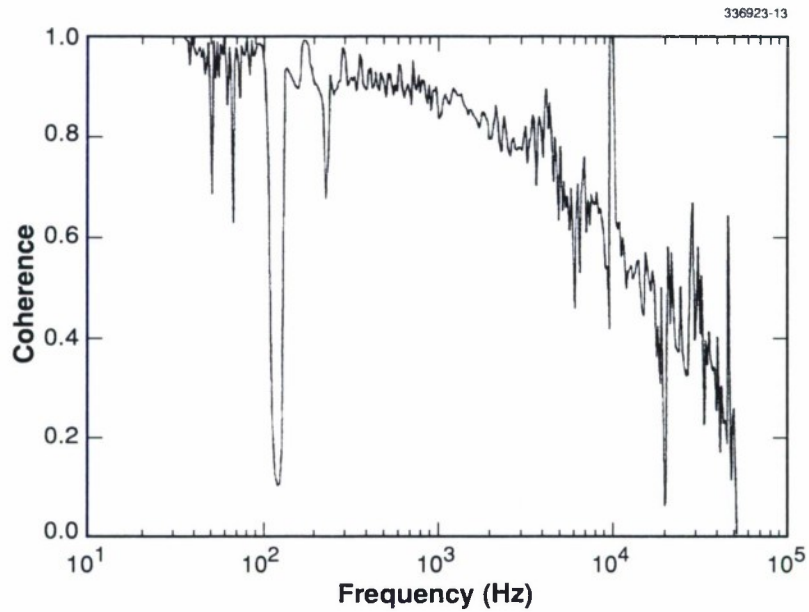
Figure 5-2. Plot of coherence vs log frequency for 1/f amplitude and phase noise.

336923-14
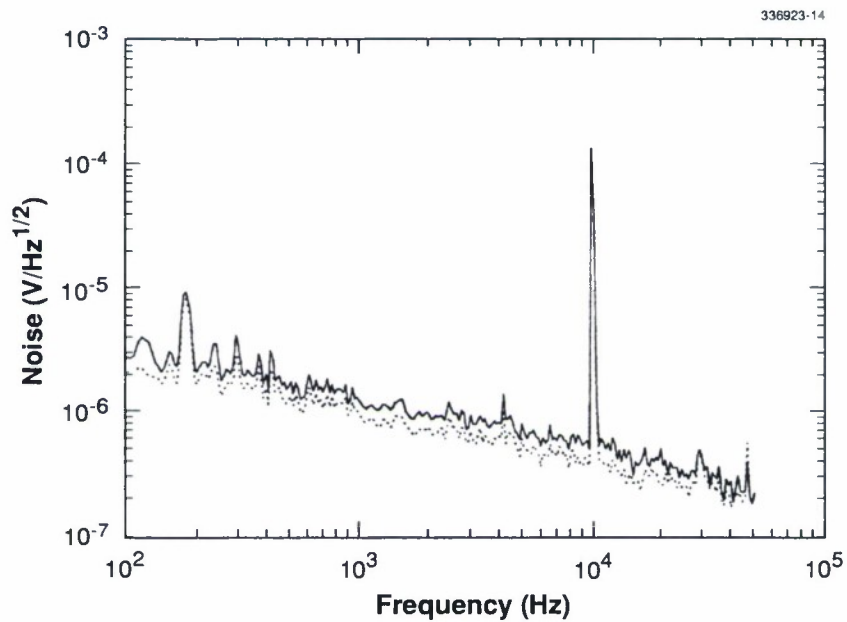
Figure 5-3. Log power spectral density vs log frequency of the baseband 1/f amplitude noise and 10-kHz amplitude signal (dotted), and the phase noise and phase-converted 10-kHz signal (solid).

REFERENCES

1. K. Takagi, S. Serikawa, and T. Kurita, *IEEE Trans. Electron Devices* **44**, 1180 (1997).

2. A. van der Ziel, *Noise in Solid State Devices* (Wiley, New York, 1986), Chap. 8.

6. ANALOG DEVICE TECHNOLOGY

6.1 TEMPERATURE DEPENDENCE OF FMR LINEWIDTH FROM RARE-EARTH IMPURITIES IN MAGNETIC GARNETS

Transmission of microwave energy is critical to the efficiency of ferrites used in control devices. Ferrimagnetic resonance (FMR) relaxation that is reflected in the linewidth ΔH can be an essential mechanism in the loss of microwave signal intensity, particularly in situations where conductor and dielectric losses are negligible. At low temperatures, conductor surface resistance can be dramatically lowered by the use of superconductors [1]. Previous investigations of spin-lattice relaxation time τ in magnetic garnets have revealed two basic features: (1) a monotonic decrease in the FMR linewidth with reducing temperatures, and (2) a marked peak in the range 30–100 K that is proportional to the concentration of fast-relaxing ions, particularly Tb^{3+}, Dy^{3+}, Ho^{3+}, Er^{3+}, and Yb^{3+} of the rare-earth series. Early attempts to analyze the exchange interaction between the fast-relaxing impurity and the tightly spin-coupled iron sublattices was not successful partly because of the unavailability of an effective molecular field computational model.

To address this problem a first-order approximation to the exchange linkage between iron ions and isolated rare-earth ions was developed from the theory of the thermomagnetization properties of rare-earth iron garnets [2]. Paramagnetic relaxation theory is applied directly to produce estimates of the FMR relaxation rates, which are translated into FMR linewidths according to the conventional damping theories [3].

If the problem of linewidth broadening is viewed from the perspective of conventional FMR theory, the intrinsic ΔH is related to the spin-lattice relaxation by simply $\Delta H \approx 1/\gamma\tau$ with $\gamma = 2.8$ GHz/kOe. The intrinsic (free precession) linewidth is determined by the effective value of τ^{-1} and its dependence on T, which also influences exchange coupling below the Curie temperature. If relaxation rates are transition probabilities, a straightforward addition of the respective relaxation rates τ_{Fe}^{-1} and τ_{RE}^{-1} for the net iron and rare-earth ions can be used according to [4]

$$\frac{1}{\tau} = \frac{1}{\tau_{Fe}} + \zeta \frac{1}{\tau_{RE}} \tag{6.1}$$

or

$$\Delta H = \Delta H_{Fe} + \zeta \Delta H_{RE} \quad , \tag{6.2}$$

where ζ is a factor that is proportional to the concentration of rare-earth ions and the energy of their exchange coupling to the iron sublattices. The individual relaxation times can be expressed as $\tau_{Fe} \sim T^{-n}$ ($\sim 10^{-7}$ s at 300 K) and $\tau_{RE} \sim \exp(D/kT)$ ($\sim 10^{-13}$ s at 300 K), where $n \sim 2$ and D is the splitting energy of the lowest excited state of the rare-earth multiplet.
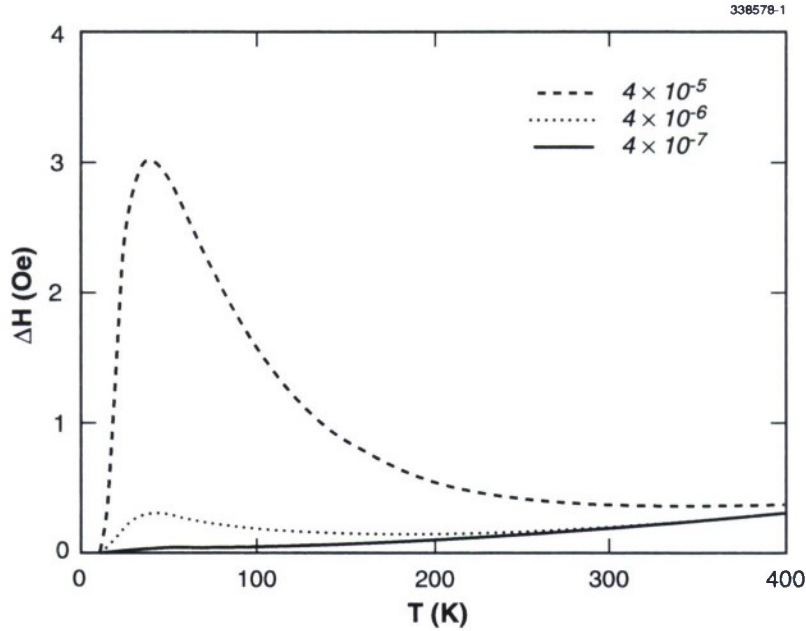
Figure 6-1. Theoretical estimates of ferrimagnetic resonance linewidth vs temperature for three Dy impurity concentrations in YIG.

In previous attempts to interpret ΔH vs T data, difficulty was encountered in explaining the decrease above the temperature of the ΔH peak. All theories of τ^{-1} hold that relaxation rates increase with T and therefore the positive low temperature slope is intuitively accepted. As T increases, ΔH is caused to decrease by the reduction in the parameter ζ due to the weakening in the exchange coupling computed by the molecular field theory.

From a practical standpoint, this study leads to a conclusion that purification of Y_2O_3 can produce substantial improvements in microwave device efficiency at low temperatures. From calculated curves in Figure 6-1, we conclude that the highest purity Y_2O_3 should be used for low-loss YIG-based microwave devices that operate in the temperature range below 100 K. Commercially available Y_2O_3 with purity sufficient for this purpose can be obtained at reasonable cost. Furthermore, compositions of reduced yttrium content can be designed with calcium, vanadium, and indium substitutions.

G. F. Dionne
G. L. Fitch

38

REFERENCES

1.   G. F. Dionne, D. E. Oates, D. H. Temme, and J. A. Weiss, *IEEE Trans. Microwave Theory Tech.* **44**, 1361 (1996).

2.   G. F. Dionne and P. L. Tumelty, *J. Appl. Phys.* **50**, 8257 (1979); also G. F. Dionne, Magnetic Moment versus Temperature Curves of Rare-Earth Iron Garnets, MIT Lincoln Laboratory Technical Report 588, 1981. AD-A107898/9

3.   K. J. Standley and R. A. Vaughan, *Electron Spin Relaxation Phenomena in Solids* (Plenum, New York, 1969).

4.   G. F. Dionne, *IEEE Trans. Magn.* **28**, 3201 (1992).

7. ADVANCED SILICON TECHNOLOGY

7.1 A DETERMINISTIC FRAMEWORK FOR NATURAL LANGUAGE PROCESSING

A method of grammatical parsing of natural language discourse is described that permits discourse-related analysis to be performed in tandem with the parsing. This method effectively blurs the distinction between syntactic and discourse-related issues at the system level. We believe that this makes for a valuable approach to discourse analysis, alternative to approaches that utilize functionally separate syntax and discourse analysis modules. In a moment, we will describe an example of the application of our approach to indirect noun phrase coreference.

In essence, our scheme involves modifying Marcus's deterministic parsing algorithm [1] so that, instead of manipulating words which carry little more in the way of linguistic features than part-of-speech tags, the modified engine, called STAX, manipulates lexical tokens that have the structure of Minsky-like frames [2]. Such a frame can be thought of as a table whose rows, or slots, carry default expectations about the syntactic and semantic roles that the associated word might play in the discourse. Our modification to the Marcus engine involves "overloading" the "attach" operation (i.e., the parser operation wherein a syntactic constituent is appropriately attached to the parse tree under construction) so that when syntactic attachment is performed, discourse-related attaching is performed as well.

The grammar that we used in this exercise is simply Marcus's original grammar [1]. An example of the sort of analysis STAX is able to perform is illustrated by considering the following example, which involves indirect noun phrase coreference:

1a. Joe walked into the kitchen.
1b. He turned off the gas.

In addition to providing a syntactic parse of each sentence, and determining that *Joe* and *He* corefer, STAX provides as part of its output a frame whose slot values indicate that the *kitchen* probably contains a stove, that the stove probably runs on *gas*, and that it is probably this *gas* that *Joe* has *turned off*. This determination of indirect coreference is made by a search through the frame-based lexicon, following links determined by the content in the frame slots of the lexical items. The search is triggered by the fact that *the gas* is a definite article noun phrase, which therefore is likely to have a prior referent.

Here are two typical lexical entries:

```
{
kitchen
IsAKindOf:  room
HasAsPart:  stove
HasAsPart:  refrigerator
HasAsPart:  sink
}
```

```
{
stove
PartOf: kitchen
Uses: gas
Uses: electricity
}
```

Our original hope was that lexical information could be extracted from WordNet [3], an online lexicon, and used with very little modification, but we have found it necessary to add, by hand, so-called deep case values such as these examples indicate. The deep case tags, such as IsAKindOf, represent fundamental semantic relationships that exist, at least in some default sense, between words. The deep case values impose a network structure on the lexicon in a well-known way: The lexical item *kitchen* points to the item *stove* through a HasAsPart-link; *stove* points to *gas* through a Uses-link.

With regard to the actual slot values, note that although a kitchen may contain a different set of objects from stoves, refrigerators, and sinks, and although stoves aren't necessarily parts of kitchens and do not necessarily run on electricity or gas, these lexical entries nonetheless contain reasonable default expectations, in the spirit of Minsky frames. The nodes in the semantic network constituted in this way by the lexicon are called lexical templates; they are to be understood as concepts — the concept of stove, the concept of gas, and the like — rather than any particular stove or gas appearing in the discourse. As such, their attributes represent expectation rather than reality. When the discourse refers to some actual stove — that is, when STAX must deal with stove as a so-called discourse entity rather than as an abstract concept — a copy of the lexical template stove is made, and this copy, called a lexical instance, is subject to having its default slot values overwritten with data representing the reality of the discourse. Here is an example illustrating this principle:

2a. I gazed at the stove.
2b. It still looked beautiful, even though it was in a junkyard.

Toward the end of the parse of 2a, when *the stove* is attached to the parse tree to complete the prepositional phrase *at the stove*, a discourse entity for this particular stove is created. This means that a copy of the lexical template stove is made. This copy, which we are calling a lexical instance, contains default slot values, because we do not at this point have any discourse-specific information about this particular stove. So, for example, the lexical instance stove contains a PartOf-link to the lexical template kitchen, and the interpretation of this link is that this actual stove is presumably sitting in some as-yet-unspecified kitchen. At the end of the parse of 2b, however, when the phrase *in a junkyard* is attached to the parse tree, we see (through reference by *it*, and the fact that *in* designates location) that our particular stove is actually in a junkyard and not in a kitchen. At that point, a new PartOf-link will be established between the lexical instance junkyard and our lexical instance stove. This newly established link overwrites the default PartOf-link that had existed between the lexical template kitchen and our lexical instance stove.

STAX also maintains frames that represent discourse entities. The slots of such a frame simply constitute a list of those lexical instances that refer to the entity in question. For instance, in Example 1, the

42

lexical instances Joe and He refer to the same discourse entity, presumably some agent named Joe who is assumed by default to be a person, and are bound together as slot values in a frame for that purpose.

This work is an initial effort to bring as much semantic and discourse-related analysis as possible under the umbrella of the kind of deterministic parsing first characterized by Marcus [1], and extended and applied in various ways since then; for example, see Ref. 4. (I will refer to the classical Marcus algorithm henceforth as CM.) The system advantages we anticipated are simplification, unification, and the kind of perspicuity that is associated with nondeterministic left-to-right parsing. (One presumably makes this latter association because such a process mimics the appearance of human acquisition of discourse.)

In CM, the algorithm employs two data containers, the "stack" and the "buffer." In the (infinite) stack, the algorithm attempts to build a constituent (such as a prepositional phrase) of the grammatical parse tree of the sentence under analysis by attaching the appropriate children to this constituent. The potential children reside in the (typically three-element) buffer, and are either incoming words being read from the input sentence, or previously created constituents. When a constituent is complete, it is popped off the stack and pushed into the buffer, whence it becomes available to be attached as a child in the construction of the next higher constituent. This attaching is the main operation that takes place in this algorithm, and the way that it works is by the application of "pattern-action rules." These rules actually constitute the grammar in such a parser as CM. In the course of a parse, when a particular rule's pattern is matched, then that rule's action is triggered. The kinds of patterns to be matched are part-of-speech values of entries in the stack and buffer. For example, a particular rule's pattern might be: "The first buffer element is an article and the second buffer element is a noun." There are various possible actions that can be taken, but the attach action is of particular interest to us: A word or syntactic constituent that has not yet been attached to the parse tree is hereby attached at some specified location in the tree. For example, an action might be: "Create a noun phrase node at the top of the stack. Attach the first buffer element to this noun phrase as a determiner. Attach the second buffer element to this noun phrase as a noun."

Two further points about pattern-action rules are in order. First, the rules are actually written in a stripped-down modification of English that Marcus calls "pidgin." For example, the rule above would actually be written:

[det]
[noun]
→
Create an NP.
Attach 1st to C as det.
Attach 2nd to C as noun.

Here, C refers to the top of the stack. For purposes of exposition, we will continue to present examples of rules in ordinary English. The second point is that the rules have fixed priorities, so that if two rules have patterns that both match a certain situation, the rule with the higher priority (which is presumably the rule whose action is likely to be the more appropriate action) is the rule actually invoked.

Since the pattern-matching facility in the Marcus parser normally attempts to match a word or constituent's part of speech, the discourse that one inputs to this parser must be preprocessed by a part-of-speech tagger; in our case, we used Brill's tagger [5]. Our concept in extending CM is that if matching could take place that were to go beyond part-of-speech pattern matching, then accordingly, attaching could take place that goes beyond basic syntactic attachment. In the STAX implementation, this extra-syntactic pattern-action activity takes place whenever the syntactic attach action is triggered. Conceptually, when a constituent is to be attached syntactically to the parse tree, STAX asks what other sorts of attachment might also be made at the same time. These other attachments, once made, take the form of slot entries in appropriate frames.

An informal walkthrough of part of the STAX process, using Example 1, will serve to make these ideas more concrete. At a certain point late in the parse of sentence 1b, a grammatical pattern-action rule called Objects looks for a constituent in the first buffer position having the pattern: "A noun phrase." It finds a match in the noun phrase *the gas*. The parser then performs the action specified by the rule Objects, which is: "Attach *the gas* as a noun phrase to the constituent currently under construction at the top of the stack." That constituent happens to be the verb phrase *turned off*, which after attachment becomes the verb phrase *turned off the gas*. Under our extension of CM, this syntactic attachment triggers a module which tests a set of extra-syntactic pattern-action rules. The first such rule, in priority order, for which there is a match, is called Definite-Indirect. It has the pattern: "The just-attached constituent is (1) a definite-article noun phrase, which (2) is referenced indirectly in the previous clause." This pattern is matched by *the gas*, whence the appropriate action is taken. That action is: "Determine the coreferent antecedent of this definite-article phrase." In this case, the action is a side effect of verifying part (2) of the pattern. This verification/action is carried out by traversing the semantic network structure imposed on the lexicon by the frame-slot values of entries in the lexicon. In this case, the relevant entries in the lexicon, as listed above, are:

```
{
kitchen
IsAKindOf: room
HasAsPart: stove
HasAsPart: refrigerator
HasAsPart: sink
}


{
stove
PartOf: kitchen
Uses: gas
Uses: electricity
}
```

Recall that STAX creates, in standard fashion, a semantic network from the lexicon, which will contain a HasAsPart-link from the lexical instance kitchen to the lexical template stove, and a Uses-link from the lexical template stove to the lexical instance gas. As part of the verification/action of the rule Definite_Indirect, STAX (1) attempts to determine if there is some path in the semantic network between *kitchen* and *gas*; (2) determines as we have indicated that there is; and (3) creates a new frame with slot values filled so as to indicate that *kitchen* and *the gas* stand in the previously noted relationship, whose meaning can be expressed: The *kitchen* probably contains a stove, that stove probably runs on *gas*, and it is probably this *gas* that *Joe* has *turned off*.

Let's walk through Example 1 again, but this time let's trace the events that lead STAX to the determination that *He* and *Joe* corefer. At a certain point early in the parse of sentence 1b, STAX determines that *He* matches the pattern of a grammatical rule called Unmarked-Order. That pattern is: "A noun phrase." STAX then carries out the action required by Unmarked-Order, which is: "Attach that noun phrase to the constituent currently under construction," which in this case is sentence 1b itself. As before, this attach-action triggers a STAX module that tests a set of extra-syntactic pattern-action rules. The first of these rules, in priority order, for which there is a match, is called Personal-Unique. It has the pattern: "The just-attached constituent is (1) a personal pronoun, which (2) has a unique referent in the previous clause." *He* matches this pattern, so the action of the rule is carried out. That action is: "Find the discourse entity to which the pronoun refers." In this case, as before, the action is a side effect of verifying part (2) of the pattern. To see how the verification/action of Personal-Unique is carried out, recall that discourse entities, themselves represented by frames, are created whenever noun phrases are encountered, unless those noun phrases refer to previously encountered discourse entities. The frame acts as a header of the list of noun phrases which are considered to constitute the entity. In this example, when *He* is encountered, STAX searches through existing discourse entities to see whether *He* refers to such an entity. That entity whose only noun phrase element is *Joe* is chosen, since it is the only semantically reasonable choice in this example. The noun phrase *He* is joined to that discourse entity, thus annotating the fact that *Joe* and *He* corefer.

This example was sufficiently simple that the typical ambiguity one encounters in resolving pronoun reference was not present. The way such ambiguity is handled in STAX is by guiding the search according to one of the current versions of centering theory [6]. Centering theories in general are intended to provide algorithms to determine the focus or central topic of any clause in a discourse. These theories tend to provide, as a side effect, guidance in resolving problems of pronoun coreference. The particular version of centering that we employ was chosen for this prototype because of its simplicity. The STAX framework is certainly amenable to more sophisticated algorithms, such as the implementation of RAFT/RAPR (Revised Algorithms for Focus Tracking and Revised Algorithms for Pronoun Resolution) [7] in the PIE (Principar-driven Information Extraction) system [8]. The way that we implement centering is by assigning priorities to the relevant extra-syntactic pattern-action rules in such a way as to mirror the rules of centering theory. In simplified form, the details of the version of centering implemented in STAX are that for each clause in a discourse, one has an ordered list of discourse entities called forward looking (FL) centers, which are referenced in that clause. The ordering is something akin to the order in which the discourse entities are encountered in a parse tree of the clause. Thus, subject would precede object in a simple declarative sentence, and they would each precede the objects in any modifying prepositional phrases. A particu-

45

lar one of the FL centers which is coreferenced in the previous clause is called the backward looking (BL) center. The idea is that the BL center represents the focus of the discourse in its containing clause. In any particular clause, one orders the FL centers and chooses the BL center according to a scheme of constraining conditions. For example, one of these conditions is as follows:

> The BL center is chosen to be that member of the present clause's FL centers which is also a member of the previous clause's FL centers, and which is as high as possible in the list of the previous clause's FL centers.

To see how this condition applies, consider this example:

3a. Lyn races Susan on weekends.
3b. She races Jack during the week.

She is the only discourse entity in 3b that also appears in 3a. We associate *She* with *Lyn* rather than with *Susan* in order to satisfy the above-stated centering condition. This is a simple illustration of the use of centering theory in the task of pronoun resolution. Centering theory actually has several conditions that come into play in a more complex fashion, given more complex examples. Again, the priorities among the relevant set of extra-syntactic rules in STAX are chosen so as to implement this more-complex behavior.

We have described a prototype system, STAX, which we have built with the goal of testing the effectiveness of a new architecture for systems in which syntactic and discourse-related analysis are to be combined. We believe that, aside from leveraging the perspicuity of the Marcus algorithm's left-to-right parsing style, this approach provides advantages, demonstrably in the area of indirect noun phrase coreference, that arise from the blurring of syntactic and discourse-related issues at the system level.

<div align="center">R. S. Frankel</div>

REFERENCES

1. M. Marcus, *A Theory of Syntactic Recognition for Natural Language* (MIT Press, Cambridge, Mass., 1980).

2. M. Minsky, "A framework for representing knowledge," in *The Psychology of Computer Vision* (MIT Press, Cambridge, Mass., 1975), p. 211.

3. G. Miller, "WordNet: An online lexical database," *Int. J. Lexicogr.* 3 (4), 1990.

4. D. Hindle, "Deterministic parsing of syntactic non-fluencies," *Proceedings of the Association for Computational Linguistics* (ACL, New Brunswick, N.J., 1983).

5. E. Brill, "A simple rule-based part of speech tagger," *Proceedings of the Third Conference on Applied Computational Linguistics* (ACL, New Brunswick, N.J., 1992).

6. S. Brennan, L. Friedman, and C. Pollard, "A centering approach to pronouns," *Proceedings of the Association for Computational Linguistics* (ACL, New Brunswick, N.J., 1987), p. 155.

7.   L. Suri and K. McCoy, "RAFT/RAPR and centering," *Comput. Ling.* **20** (2), 301 (1994).

8.   D. Lin, "Description of the PIE system used for MUC-6," *Sixth Message Understanding Conference Proceedings* (Morgan Kaufmann, San Francisco, 1995), p. 113.

REPORT DOCUMENTATION PAGE

1. AGENCY USE ONLY (Leave blank)	2. REPORT DATE 15 November 1999	3. REPORT TYPE AND DATES COVERED Quarterly Technical Report, 1 August–31 October 1999

4. TITLE AND SUBTITLE

Solid State Research

6. AUTHOR(S)

David C. Shaver

5. FUNDING NUMBERS

C — F19628-95-C-0002

7. PERFORMING ORGANIZATION NAME(S) AND ADDRESS(ES)

Lincoln Laboratory, MIT
244 Wood Street
Lexington, MA 02420-9108

8. PERFORMING ORGANIZATION REPORT NUMBER

1999:4

9. SPONSORING/MONITORING AGENCY NAME(S) AND ADDRESS(ES)

HQ Air Force Materiel Command
AFMC/STSC
Wright-Patterson AFB, OH 45433-5001

10. SPONSORING/MONITORING AGENCY REPORT NUMBER

ESC-TR-99-060

ADA 377032

11. SUPPLEMENTARY NOTES

None

12a. DISTRIBUTION/AVAILABILITY STATEMENT

Approved for public release; distribution is unlimited.

12b. DISTRIBUTION CODE

13. ABSTRACT (Maximum 200 words)

This report covers in detail the research work of the Solid State Division at Lincoln Laboratory for the period 1 August–31 October 1999. The topics covered are Quantum Electronics, Electro-optical Materials and Devices, Submicrometer Technology, Biosensor and Molecular Technologies, Advanced Imaging Technology, Analog Device Technology, and Advanced Silicon Technology. Funding is provided by several DoD organizations— including the Air Force, Army, BMDO, DARPA, Navy, NSA, and OSD — and also by the DOE, NASA, and NIST.

14. SUBJECT TERMS

quantum electronics	biosensor technology	semiconductor lasers	bioelectronic sensors
electro-optical devices	advanced imaging technology	thermoelectric materials	buried channel transistors
materials research	analog device technology	lithography modeling	microwave devices
submicrometer technology	advanced silicon technology	ion mobility spectroscopy	natural language processing

15. NUMBER OF PAGES

73

16. PRICE CODE

17. SECURITY CLASSIFICATION OF REPORT	18. SECURITY CLASSIFICATION OF THIS PAGE	19. SECURITY CLASSIFICATION OF ABSTRACT	20. LIMITATION OF ABSTRACT
Unclassified	Same as Report	Same as Report	Same as Report